RESEARCH ARTICLE | DECEMBER 17 2024

Magnetic soliton-based LIF neurons for spiking neural networks (SNNs) in multilayer spintronic devices

Kishan K. Mishra

AIP Advances 14, 125119 (2024)
https://doi.org/10.1063/5.0232395

Magnetic soliton-based LIF neurons for spiking neural networks (SNNs) in multilayer spintronic devices

Cite as: AIP Advances 14, 125119 (2024); doi: 10.1063/5.0232395
Submitted: 8 October 2024 • Accepted: 27 November 2024 •
Published Online: 17 December 2024

Kishan K. Mishra[a]

AFFILIATIONS

Department of Physics and Astrophysics, University of Delhi, Delhi, India

[a]Author to whom correspondence should be addressed: 20025762025@physics.du.ac.in and Physics.kishan@gmail.com

ABSTRACT

Neuromorphic computing, inspired by biological nervous systems, is gaining traction due to its advantages in latency, energy efficiency, and algorithmic complexity compared to traditional artificial neural networks. This has spurred research into artificial synapses and neurons that replicate brain functions. Spintronic-based technologies, particularly domain walls (DWs) and skyrmions (SKs), have shown remarkable potential for brain-inspired computing, facilitating energy-efficient data storage and advancing beyond CMOS computing architectures. Researchers have proposed various DWs- and Sks-based neuromorphic architectures for neurons and synapses. Leveraging magnetic multilayer structures, we propose a magnetic soliton that incorporates both DWs- and Sks-based magnetic tunnel junction (MTJ) device structures to emulate leaky integrate-and-fire (LIF) characteristics. These characteristics are controlled by spin–orbit torque (SOT)-driven motion within ferromagnetic thin films. By strategically placing the reading block and utilizing a combination of SOT and varying demagnetization energy, we achieve modified LIF neuron characteristics in both DW and Sks MTJ devices. The co-action of soliton dynamics across the nanotrack during the application of the current pulse, along with edge repulsion and variations in demagnetization energy, exploits LIF spiking behavior. Theoretical and micromagnetic analyses reveal that the transitory tunable positions of Sks and the total magnetization of the free layer for DWs mimic the membrane potential of biological neurons. Initial studies on multilayer DW-based LIF characteristics showed promise; however, maintaining leaky behavior required a constant negative current, which is energy inefficient. By incorporating the non-volatile properties of skyrmions and adding a chiral Dzyaloshinskii–Moriya interaction term, we further explored LIF dynamics, yielding encouraging results. Our proposed neuron model, implemented in fully connected and convolutional layers, achieves over 95% classification accuracy on the MNIST and Fashion MNIST datasets using a modified spike-based backpropagation method. With nanosecond latency, these spiking neuron devices, when integrated with CMOS, pave the way for high-density, energy-efficient neuromorphic computing hardware.

I. INTRODUCTION

Quantum computing[1] and neuromorphic computing[2] are pioneering computing stages that emerged to address the limitations of classical computing, but they do so in fundamentally different ways. Quantum computing that is deeply rooted in the principles of quantum mechanics utilizes semiconductor/superconductor qubits[3] and phenomena such as superposition and entanglement to perform computations that can vastly outperform classical computers in specific tasks such as factoring large numbers or simulating quantum systems. This field gained significant momentum in the 1980s with the development of quantum algorithms by pioneers such as Feynman[4] and Deutsch and Ekert.[5] Pioneered in the late 1980s, neuromorphic computing,[2,6] brain-inspired extremely energy efficient computing, which mimics the human brain computation architecture, leverages spiking neural networks[7–11] and CMOS-based custom hardware like neuromorphic chips such as IBM's TrueNorth[12] and Intel's Loihi[13] to efficiently process sensory data and perform tasks related to perception,[14] image classification,[15] pattern recognition,[16–18] and machine learning.[19] Both fields are converging toward creating new computing paradigms that aim to surpass traditional capabilities, with quantum computing

promising exponential speed-ups for certain problems[20] and neuromorphic computing offering unparalleled efficiency, robustness for real-time processing, scalability, integration,[21] and adaptive tasks.[7] In the past two decades, extensive research has been carried out on various materials to develop structures for this purpose. These include resistive random-access memory (RRAM),[22] phase change materials (PCM),[23,24] ferroelectric materials,[25] and spintronic devices[26] specific to our case. Among these, spintronic devices[27–29] due to their ultra-fast dynamics and high endurance toward the advancement of data storage devices and energy-efficient computing architecture for much promising future are considered the most promising for neuromorphic computing. The advantage of considering spintronic devices is the feasibility of developing all counterparts and transistor circuits (such as memory, logic, neurons, and synapses). A multitude of spintronic technologies has made significant progress in unconventional computing architectures such as neuromorphic computing,[16,30,31] probabilistic computing,[32] and reservoir computing paradigms.[33] More recently, a branch of spintronic that pursued studying magnetic solitons, such as domain walls (DWs),[34] vortices,[35] skyrmion (Sks),[36–38] and hofion,[39] have been extensively explored for next building blocks for data storage,[40] memory applications, and processing units.[37] Magnetic domain walls (DWs) and skyrmions (Sks) are experimentally stabilized topological solitons in a ferromagnetic thin film system when different magnetic energy terms, such as magnetic anisotropy, exchange energy, stray field energy and Dzyaloshinskii–Moriya interaction (DMI), compete with each other to attain the energy minima.[41] The stabilization of stripe-like domain walls and skyrmions has been observed in several noncentrosymmetric materials, as well as in ferromagnetic heterostructures such as $(Co/Pt)_n$ $(CoFeB/Pt)_n$ and $(CoFeB/Ta)_n$.[42,43] However, achieving precise control over the dynamics, stability, and detection of these materials remains challenging due to their topological nature and the spin Hall effect. Since the development of current-induced spin-transfer torque (STT)[44] and spin–orbit torque (SOT),[45] as well as the application of external magnetic fields, solitons and their dynamics can be detected through changes in resistance states[46] known as magnetoresistance or the topological Hall effect and by performing advanced computational measurements such as magnetic force microscopy (MFM), small-angle neutron scattering (SANS), and Lorentz transmission electron microscopy (LTEM). Magnetic domain walls (DWs) and skyrmions (Sks) have been extensively explored for applications in racetrack memory devices,[47] MRAM, logic devices,[48] non-volatile circuits,[49] spin-valve and magnetic tunnel junctions (MTJs),[50] and nano-oscillators.[51] Compared to STT in MTJs, where the current passes through the junction, SOT allows the magnetization of a ferromagnet to be manipulated by current flowing transversely to a ferromagnetic/nonmagnetic bilayer. SOT is stronger and faster than STT-driven magnetization switching.[52] The movement of the domain wall creates variations in the net magnetization of the MTJ-free layer, resulting in analog MTJ resistance switching characterized by tunneling magnetoresistance (TMR).[53] For instance, (CoFeB/MgO) structures have demonstrated improved TMR ratios (>200% at room temperature) while maintaining relatively low read and write voltages (~0.5 V), highlighting the promise of this technology.[54,55] Among spintronic devices, DW-MTJs leveraging DW dynamics, which can be precisely manipulated by electrical methods,[56–59] are ideal candidates for applications in neural networks for both linear weight updating and non-linear activation functions due to their intrinsic linear relationship between junction magnetoresistance and programming stimuli.[60] Similarly, magnetic skyrmions, which are topologically stable magnetic textures[61] found in bulk ferro-magnets[62] or ultrathin ferromagnetic films,[63] are established by a chiral Dzyaloshinskii–Moriya interaction (DMI) originating from strong spin–orbit coupling (SOC) and broken inversion symmetry.[64] Skyrmions are small,[36] ultra-dense, and require low driving current for their propagation compared to domain walls.[65] Recently, the generation and manipulation of stable magnetic skyrmions have been demonstrated experimentally at room temperature,[63,66,67] which further highlights the opportunity for novel applications.

It is these remarkable properties that make them an ideal candidate for racetrack memory devices,[36] reservoir computing,[68] and neuromorphic computing so they can accumulate, aggregate, and fire in a probabilistic manner.[46,69] Several proposals have been made for domain wall and skyrmion-based spiking neural networks (SNNs) including skyrmion-based neuromorphic synaptic devices,[69] skyrmion-based artificial neurons,[17] and skyrmion-based leaky integrate-and-fire (LIF) neurons.[70–72] Despite advancements, controlling skyrmion motion in devices, managing its dynamics, and achieving precise detection remains a setback because the current density must be above the depinning level due to the skyrmion Hall effect. In particular, neuromorphic computing technologies have leveraged magnetic domain wall and skyrmion-based magnetic tunnel junction structures[67,73] to mimic synaptic and neuron behaviors in artificial neural network architectures.[16,69] Domain wall-based neuromorphic devices exhibit bio-plausible linear and symmetric relationships between synaptic weights and pulses, demonstrating their potential in synaptic functionality.[74–78] However, considerable challenges persist in terms of scalability, latency, and integration with CMOS device structures. In this work, we provide more tunable and versatile magnetic multilayer (MML) DW-MTJ and skyrmion-MTJ-based spintronic devices, with optimized device geometries showing leaky-integrate and fire (LIF) neuron characteristics and their implementation into spike neural networks.

This paper is structured as follows: first in Sec. II, we provide a detailed discussion of the micromagnetic simulated MML structure of the LIF neuron device. The multilayer structure that consists of CoFeB/Ta exhibits DW and skyrmion motion in the presence of SOT when analyzed individually. The use of highly stable topological solitons, such as domain walls (DWs) and skyrmions (Sks), which are ultra-small, is crucial for high-density integration and helps address scalability issues. The MTJs perform the reading of DW and skyrmion, showcasing DW/SK-MTJ-based devices. In addition, employing MML and SOT dynamics can improve latency challenges, which stem from the time required for skyrmion nucleation, movement, and detection, thereby enhancing the overall speed and efficiency of the neuromorphic system. We have thoroughly analyzed the multilayer by spanning from 3 layers to 20 layers, the effect of the dynamics and the LIF characteristics using micromagnetic simulation mumax[79] and Python libraries. Next, in Sec. III A, we emphasize the developed neuron models and their LIF characteristics, accompanied by a brief yet comprehensive analysis of biological, artificial, and spiking neurons. Owing to the field, more recently significant research has been spurred in the area of spiking neural networks SNNs,[7–11,15,80,81] which are considered to be having

more biological plausibility. Spiking neural networks (SNNs) are computational models that process information based on spikes generated by spiking neurons. Unlike traditional artificial neural networks that operate continuously, SNNs use discrete time events or "spikes," making them more energy-efficient and effective for event-driven AI tasks on edge computing. This spatiotemporal data encoding in SNNs enhances energy efficiency and performance for real-time applications.[82,83] The modeling of these neurons and the derivation of the LIF equations are achieved through analysis of the micromagnetic simulation results, leading to the formulation of the mathematical equations for the LIF model. Finally, in Sec. IV, we discuss the network architecture implemented for dataset classification and present the obtained results. Furthermore, we integrate the developed neuron models in the three-layer spiking neural network (SNN) and convolutional CSNN framework to test these spiking neuron models for the classification of the MNIST and FMNIST datasets. In both architectures, the network achieves classification accuracy above 96%. The research provides a new way to build skyrmion-based SNN for complicated pattern recognition tasks, which paves the way for the practical application of skyrmionics and can be used as an alternative to traditional CMOS-based SNN implementation. In addition, the LIF neuron latency is in ns, thus when integrated with the CMOS, the proposed device structures and associated systems exhibit a good future for energy-efficient neuromorphic computing.

II. MAGNETIC DOMAIN WALL AND SKYRMION LIF NEURON DEVICE STRUCTURE

One of the key reasons for opting for an MML device structure over a monolayer is the notable enhancement in stability against thermal fluctuations and external perturbations when increasing the number of layers from 1 to 15.[84–87] This multilayer configuration enables easier manipulation at smaller scales, offering improved magnetic memory technologies' scalability. To assess the feasibility of multilayer spintronic devices' functioning as leaky integrate-and-fire (LIF) neurons in spiking neural networks, achieving both scalability and enhanced output signals is essential.[11,88–91]

The fundamental principle can be illustrated by the simplified computational model shown in Fig. 1. Input spikes (U_i) from pre-neurons are modulated by weights (W_i) stored in the interconnecting synapses. The outputs from all synapses are summed and fed to the post-neuron through a non-linear activation function. In response to this weighted current, a neuron's membrane potential (U_{mem}) rises but decays slowly to a resting value until the next spike is received. This behavior can be expressed as follows:[92–95]

$$\frac{dU_{\text{mem}}}{dt} = -\frac{1}{\tau_{\text{mem}}}(U_{\text{mem}} - U_{\text{rest}}) + \sum_j \delta(t - t_j)W_j, \tag{1}$$

where U_{mem} is the membrane potential (i.e., the location of the skyrmion), U_{rest} is the resting potential, W_j is the synaptic weight for the jth input, τ_{mem} is the membrane time constant, and $\delta(t - t_j)$ represents the spiking events occurring at time t_j. When U_{mem} crosses a threshold (U_{th}), the neuron emits a spike, transmitted to the next layer of neurons. The term $\sum_j \delta(t - t_j)W_j$ represents the sum of input-weighted spikes from presynaptic neurons (integral term), while $(U_{\text{mem}} - U_{\text{rest}})$ represents the leakage term.

The dynamics of multilayer domain walls (DWs) and skyrmions (Sks) have been investigated to achieve higher velocities

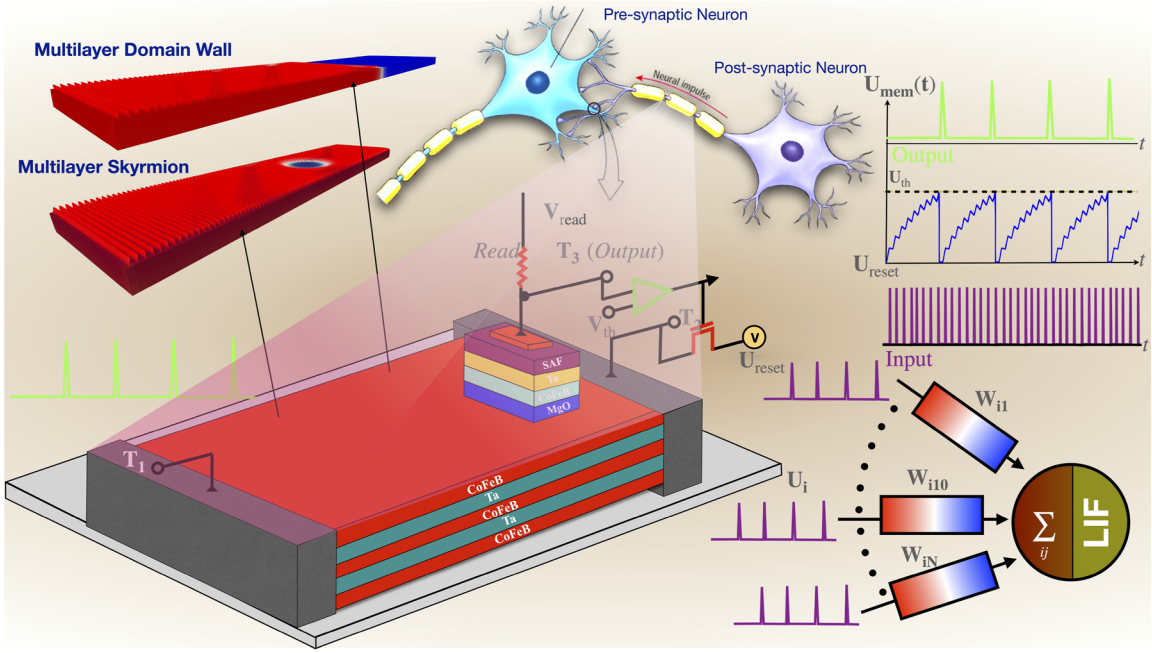

FIG. 1. Schematic of multilayer domain wall/skyrmion-based MTJ device depicting the LIF neuron behavior (top right: LIF characteristic; bottom right: synaptic connections).

and reduced sizes (multimedia available online), which is particularly important for the scalability of LIF neurons in a structure measuring 256×64 nm^2. The device consists of multilayer ferromagnetic nanotracks composed of $(Ta/CoFeB)_n$, with two terminals, T-1 (left end) and T-2 (right end), between which DWs or Sks can move. The movement of the DWs/Sks is driven by spin-transfer torque (STT) and spin–orbit torque (SOT) generated by lateral charge currents. To nucleate (or write) the DWs or skyrmions, a current pulse with an amplitude of 1×10^{11} A/m^2 and a duration of 1 ns is applied laterally to the device. To analyze the device's frequency, response pulses with varying time periods from 1.5 to 4 ns (in terms of duty cycle) are utilized. In the presence of the current pulse, DWs/Sks move from terminal T-1 to terminal T-2. The neuron's state variable, *membrane potential* (U_{mem}), is represented by magnetization in the case of DWs and skyrmion position in the case of Sks. This state is read using the tunneling magnetoresistance (TMR) effect through a magnetic tunnel junction (MTJ) reading block. Both scenarios will be individually analyzed in Subsections II A and II B using micromagnetic simulations.

A. Domain wall LIF device structure

Once a domain wall is nucleated in the device as detailed in Sec. II B and shown in Fig. 1, the current pulse is applied that generates STT and SOT that drives the DWs. The neuron's membrane potential (U_{mem}) is represented by its magnetization, which emulates the LIF behavior. As the DW moves through the free layer, it experiences edge forces, and as it nears the T2 end, the increasing demagnetization energy opposes its movement. By reading the magnetization using the MTJ near the T2 end of the nanotrack, magnetization integration in the presence of current is achieved, followed by magnetization leakage in the absence of current. The MTJ output terminal T3 is connected to the comparator for generating the magnified output spikes that propagate to the next layer. After each spike, a negative current pulse resets the membrane potential. Once the membrane potential reaches a certain threshold voltage (U_{th}), the comparator produces spikes and activates a resetting MOSFET, which allows a reverse current pulse to flow. This pulse drives the DW back to its starting position, resetting the membrane potential to its resting state (U_{rest}).

The simulated results are shown in Fig. 2. In Fig. 2(c), we see how the demagnetization energy changes over time at different writing current frequencies computed in terms of duty cycles. We initiate by nucleating the domain wall on the left side at position $X_{DW} = -200$ nm. In this position, the thin film is magnetized ~80% down ($-z$ direction) and about 20% up ($+z$ direction) with the highest demagnetization energy (E_{demag}), depicted by the magnetization evolution shown in Fig. 2(a). As the domain wall moves under the influence of competition between the repulsive force from nanotrack edge and the driving force of input spike current and reaches center, magnetization distribution of layer reaches to 50% down ($-z$ direction) and 50% down ($+z$ direction) and the demagnetization energy reduces to a minimum, as shown in Figs. 2(b) and 2(c). An explicit plot of demagnetization against variation of magnetization is shown in Fig. 2(b), where the minimum is observed at the center when magnetization is $M_z = 0$. As the domain wall propagates further away from the center to the right end of the device, the change in demagnetization energy increases further, as shown

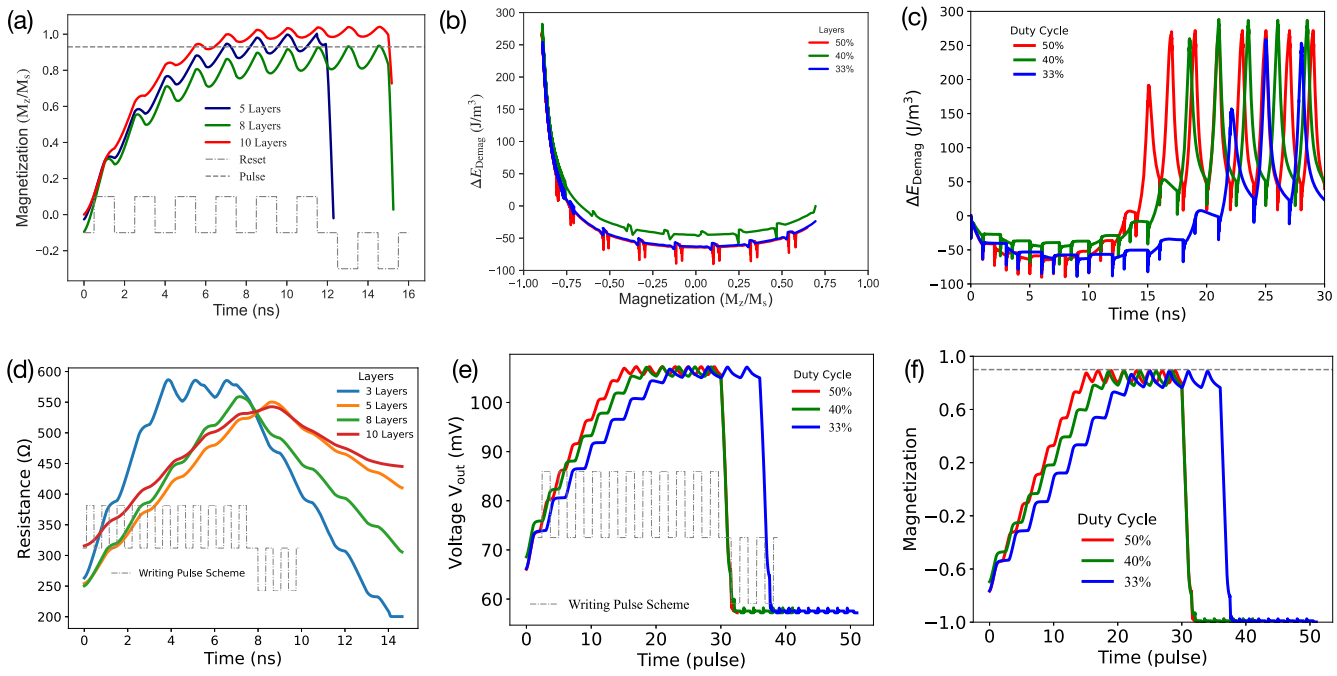

FIG. 2. Domain wall LIF results. (a) Magnetization profile of 5, 8, and 10 layer DW system; (b) ΔE_{demag} vs magnetization clearly depicts stable minima; (c) ΔE_{demag} evolves with time; (d) resistance vs time, (e) MTJ output voltage (V_{out}) vs time for duty cycle pulses, and (f) magnetization evolution for duty cycle pulses.

in Fig. 2(c), resisting the motion of DW. Figure 2(b) shows the evolution of change in demagnetization energy with the domain wall movement from T-1 to T-2. Figures 2(b) and 2(c) show the increasing demagnetization for time/magnetization for four different input pulse/spike frequencies.

We examine the variation in the multilayer energy profile, particularly focusing on the demagnetization energy. Our findings indicate that the application of current increases demagnetization due to the spin–orbit torque (SOT) on the domain wall (DW) spins. These spins are temporarily forced from a stable in-plane orientation to a perpendicular direction. When the current is switched off, the demagnetization relaxes; however, due to DW motion, the ratio of $+z/-z$ domain spins changes. This results in a shift in the demagnetization curve. Consequently, we observe (1) a transient volatile memory effect due to SOT and (2) a stable non-volatile memory effect caused by asymmetry in domain sizes.

The device's performance varies with different current pulse schemes. For a 50% duty cycle, current pulses are 1 ns ON, followed by 1 ns OFF, corresponding to a 500 MHz input frequency. For a 40% duty cycle, the ON pulse is 1 ns, followed by 1.5 ns OFF (400 MHz). For a 33% duty cycle (1 ns ON/2 ns OFF), the input frequency is 333 MHz, and for 50 MHz, the pulses are 1 ns ON/3 ns OFF. The DW reaches its threshold position in 16 ns at 500 MHz, but it takes 27 ns at 333 MHz. The demagnetization energy affects the DW's motion. As the DW approaches terminal-T2, it experiences an increasing demagnetization force. In the presence of the SOT pulse, the DW moves to the right. When the current is off, demagnetization forces cause the DW to move back, demonstrating leaky integrate-and-fire (LIF) behavior. The SOT effect is analogous to the integration of membrane potential in biological neurons, while the DW's relaxation mimics membrane potential leakage [multimedia available online, mov(a)]. As explained above, the DW motion alters the net magnetization of the magnetic tunnel junction (MTJ) free layer. In Fig. 2(f), the magnetization-time characteristics clearly show leaky integrate-and-fire behavior. At high frequencies (500 MHz), normalized magnetization (M_z/M_s) reaches the threshold value of $V_{th} = 0.9$ more quickly compared to lower frequencies such as 333 MHz. In the case of lower frequencies, such as the 33% duty cycle, the DW gets enough time to relax; thus, magnetization leakage is increased, reflected in the blue curve. The MTJ reads the magnetization change in terms of its tunnel magnetoresistance. The MTJ measures these changes as variations in tunnel magnetoresistance[76,96] as

$$\mathbf{R}_{\text{neuron}} = \mathbf{R}_{\text{AP}} \frac{[1 - \hat{m} \cdot \hat{m}_p]}{2} + \mathbf{R}_{\text{P}} \frac{[1 + \hat{m} \cdot \hat{m}_p]}{2}. \tag{2}$$

Here, $\mathbf{R}_{\text{P}}/\mathbf{R}_{\text{AP}}$ represents the MTJ resistance in a parallel/antiparallel state. Figure 2(d) shows the neuron resistance switching for 2 devices with 5 and 8 CoFeB layers. We considered the TMR 200% and $\mathbf{R}_{\text{P}}/\mathbf{R}_{\text{AP}} = 200/600$. If complete magnetization switching is considered, the V_{out} switches in the range (67–110 mV) are shown in Fig. 2(e). The resistance shown in Fig. 2(d) increases from 250 to 590 Ω in a leaky integrated behavior. For the layer-5 case, we observe fast DW switching, whereas, for the layer-8 case, the DW velocity is reduced. Thus, the threshold voltage is achieved in 15 ns.

Adding more CoFeB layers increases leakage conductance due to higher demagnetization energy, as indicated by the resistance and voltage characteristics of the eight-layer MTJ neuron shown in Figs. 2(a) and 2(d),[97]

$$V_{\text{out}} = \frac{\mathbf{R}_{\text{neuron}}}{\mathbf{R}_{\text{neuron}} + \mathbf{R}_{\text{read}}} V_{\text{read}}, \quad \begin{cases} V_{\text{out}} \geq V_{\text{th}} & : \text{spike} = 1, \\ \text{else} & : \text{spike} = 0. \end{cases} \tag{3}$$

The MTJ neuron's output (terminal T-3) is connected to a comparator with a threshold voltage (V_{th}). As the MTJ neuron voltage reaches this threshold voltage $V_{th} = 0.9$, the comparator generates the output spikes propagating to the next layer. During the firing, the reset MOSFET is also switched, allowing a current to follow from T-2 to T-1, thus driving the DW back to the initial position corresponding to the resetting of the neuron membrane voltage to its rest voltage V_{rest}. The neuron's leaky integrate-and-fire characteristics are modeled by Eq. (10) and described in detail in Sec. III A. This comprehensive analysis of the spintronic LIF neuron device illustrates its design, operation, and potential scalability, showcasing its innovative capabilities for advanced computational applications.

B. Skyrmion LIF device structure

Magnetic skyrmions, among post-CMOS technologies, have garnered significant interest due to their robustness, non-volatility, nanoscale size, and low driving threshold current density,[36,65] particularly when demonstrated at room temperature in multilayer ferromagnetic structures.[63,66] Extensive research has been conducted on their potential for low-power and highly dense neuromorphic computing applications, such as artificial neurons and synapses.[69,98,99] In Ref. 69, the concept of a skyrmion-based artificial synapse device for neuromorphic systems was initially proposed, mimicking the function of a biological synapse. For practical realization, a subsequent work introduced a novel artificial neuron model with a threshold modulated by voltage. Furthermore, deep neural network aspects of skyrmion-based devices, such as spiking neuron processors have been explored to enhance energy efficiency. Significant progress has been made in studying skyrmion-based LIF neurons in terms of device design and performance evaluation. For example, Ref. 76 investigated skyrmion dynamics driven by current in nanotracks, proposing a new LIF neuron device. Using micromagnetic simulation, Ref. 72 focused on the performance of skyrmion-based LIF neuron dynamics by injecting spin current via the CIP scheme in nanotracks, examining parameters such as size, velocity, energy, and stability. Ref. 100 explored an AFM coupled bilayer structure to mitigate the parasitic Magnus force nature of skyrmion in a track geometry depicting a skyrmion-based artificial neuron and synapse characteristics. Biskyrmion artificial neuron behavior is examined in Ref. 101, where biskyrmion splits into subskyrmion and the interaction between them leads to the integration and leakage characteristics.

Building on these achievements, we present a new method to simulate skyrmion-based LIF neurons, incorporating mathematical modeling assisted with micromagnetic multilayer simulations to validate device performance with the following device parameter presented in Table I. We have simulated 6 to 15 layer device structures with dimensions 128×64 nm^2 with thickness of 0.8 nm of each layer to thoroughly investigate the LIF state variable, specifically membrane potential behavior. Confined within the geometry, a skyrmion is nucleated at the left end of the device. Skyrmion moves

TABLE I. Material parameters used in device simulation.[71,72,114]

Parameter	Value
Grid Size	256, 64, X[a]
Cell Size (nm)	2, 2, 0.8
Anisotropy, $\mathcal{K}_u$ (J/m^2)	0.9×10^6
Saturation Magnetization, M_s (A/m)	0.8×10^6
Exchange Stiffness, $\mathcal{A}$ (J/m)	1.5×10^{-11}
DMI, $\mathcal{D}$ (J/m^2)	1.0×10^{-12}
IEC, $\mathcal{J}$ (J/m^2)	5×10^{-13}
Damping Constant, α_H	0.15

[a]X is the number of layers.

by applying the current pulses with an amplitude of 1×10^{11} A/m^2 and a width of 1 ns from terminal T-1, and various frequency responses were examined by tuning the period T from 1.5 to 4 ns. The amount of skyrmion displacement is related to the magnitude of an incoming charge current, which is modulated by the synaptic weight. The reading or detection process of skyrmion can be achieved by sensing the change in resistance arising from the presence/absence of skyrmion at a specific location in the nanotrack, i.e., tunnel magnetoresistance (TMR) effect by using a spin valve-based detector or an MTJ reading block attached to other end terminal T-2, as shown in Fig. 1, detailed in Fig. 3, and a magnetization profile is achieved as shown in Fig. 4. However, it is important to note that unlike domain wall structures, which can be read by usual MTJ P and AP states by measuring resistances, the average magnetization texture of skyrmion does not correspond to an anti-parallel ($m_z = -1$) (or parallel) to the fixed layer($m_z = 1$); a smaller magnetoresistance change is obtained. The obtained change in resistance is directly proportional to the size (diameter d_s) of the skyrmion and is inversely proportional to the cross-sectional area of the MTJ. The chances of getting a higher resistance change are better if the average magnetization detection by MTJ is closer to $m_z = -1$ (anti-parallel to the fixed layer). In the presence of an excitatory current pulse, mapping the motion of the skyrmion, i.e., *skyrmion position* X_{sk}, which mimics the biological neuron state variable: *membrane potential* (U_{mem}), characterizes the "integration" property of the LIF, while leakage occurs in the absence of a current pulse. The amount of skyrmion displacement correlates with the magnitude of the incoming charge current, modulated by the synaptic weight, as shown in Figs. 3(a) and 3(b). These combined processes define the complete characteristics of a skyrmion-based leaky integrate-and-fire (LIF) neuron. As the skyrmion progresses through the top layer from T-1, it experiences edge forces via skyrmion–edge interaction. Near the T-2 end, increasing demagnetization energy opposes its movement. The simulated results are shown in Fig. 3. In Fig. 3(c), we see how the demagnetization energy changes over time for a multilayer ferromagnetic structure.

Skyrmion is nucleated at the left end near terminal T-1 at position $X_{Sk} = -200$ nm. Under the influence of current, it moves toward the terminal T-2, depicted by the magnetization evolution shown in Fig. 3(d). Skyrmion moves under the influence of competition between the repulsive force from nanotrack edge and the driving force of input spike current and reaches center; the skyrmion position plot is shown in Figs. 3(a) and 3(b). In the presence of the SOT pulse, the Sks move to the right by overcoming the pinning and hall forces. When the current is off, restoring forces cause the Sks to move back, demonstrating leaky integrate-and-fire (LIF) behavior. The dipolar interactions within the material can also create an effective magnetic potential landscape. Skyrmions tend to settle in regions where the magnetostatic energy is minimized. When the driving current is removed, the skyrmion may move back to these energetically favorable positions. The SOT effect is analogous to the integration of membrane potential in biological neurons, while the Sk's relaxation mimics membrane potential leakage. In Fig. 3(b), the position-time characteristics clearly show leaky integrate-and-fire behavior. The characteristics are also examined by changing the width of the device, which retains the LIF behavior of skyrmion neuron, as shown in Figs. 3(g) and 3(h). After such successive integration and leakage, when the skyrmion reaches the output terminal T-3 and the resistance change read by the sensing MTJ exceeds a certain threshold (U_{th}), the inverter attached to T-3 generates a

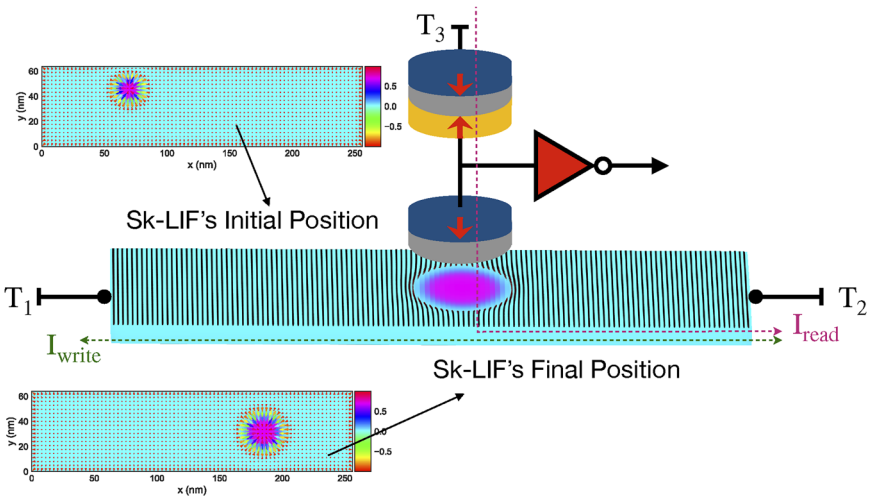

FIG. 3. Multilayer skyrmion-LIF device structure three terminals T-1, T-2 (skyrmion track), and T-3 (detection unit) as mentioned in the discussion and the MTJ to read skyrmion.

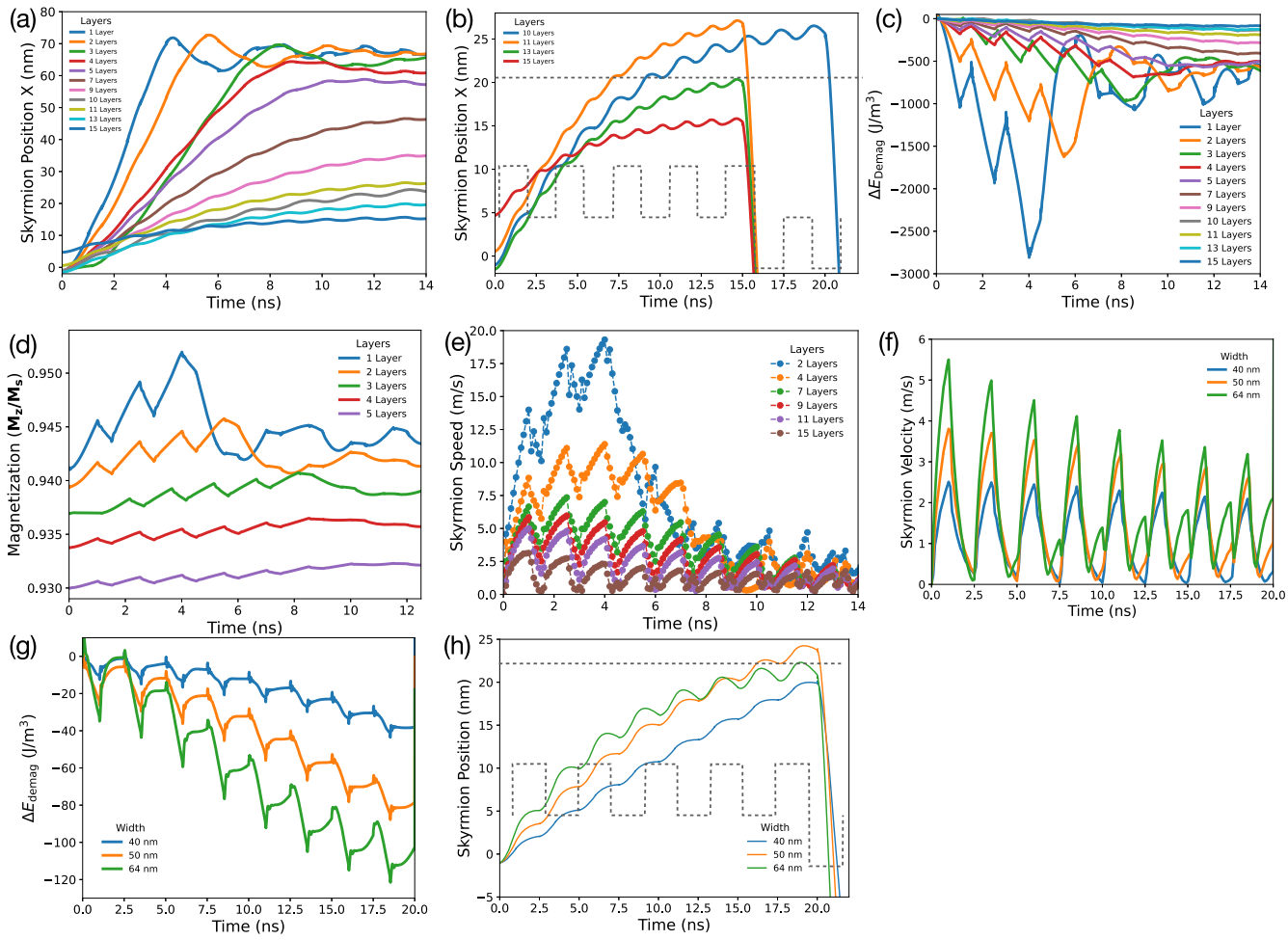

FIG. 4. Skyrmion LIF results. (a) Skyrmion position vs time for various layer device structure; (b) an enhanced Skyrmion position vs time plot for above 10 layers; (c) ΔE_{demag} vs time for various layer structure; (d) magnetization evolution for various layer structure; (e) skyrmion speed vs time; (f) skyrmion velocity dependence on devices' width; (g) ΔE_{demag} dependence on width; and (h) Skyrmion position dependence on width.

magnified output spike transmitted to the next layer. Simultaneously, the skyrmion is reset by driving it back to the origin position at terminal T-1. The resetting mechanism can be implemented in various ways: (1) when the comparator spikes, a resetting MOSFET triggers a negative current pulse in the opposite direction, driving the skyrmion to its initial position (i.e., membrane potential is reset to U_{rest}); (2) if the membrane rest potential $U_{\text{rest}} = 0$ is set by annihilating the skyrmion at the nano track edge, which is achieved by exceeding the current density to the skyrmion depinning current density and then nucleating the skyrmion at the initial position T-1, repeating the process. The nucleation, annihilation, and dynamics of the skyrmion in the nanotrack are explored in detail in Ref. 65 and briefly introduced in Sec. III B.

1. Memristive skyrmion-MTJ model

The memristive skyrmionic TMR model predicts the conductance and resistance in a magnetic tunnel junction (MTJ) influenced by skyrmions, accounting for memristive behavior.[102–104] The overall conductance G is derived as the integral of unit conductance g over the MTJ area S, taking into account the angle θ between the magnetizations of the two ferromagnetic layers. The conductance G is expressed as

$$G = g_P S - \frac{\Delta g}{2} \int (1 - \cos\,\theta)\, dS, \tag{4}$$

where g_P is the unit conductance for parallel magnetizations and Δg is the difference in conductance between anti-parallel and parallel states. This model can predict conductance based on micromagnetic simulations. To create an experimental model without specific magnetization data, it is assumed that magnetic domain walls (DWs) exist under dipolar coupling in the MTJ bilayer, influencing TMR. The term,

$$\frac{\Delta g}{2}(1 - \cos\,\theta)\, dS \tag{5}$$

is related to the skyrmion perimeter, enabling the expression,

$$G = g_P S - \pi n_s d_s \Delta g w S, \tag{6}$$

where n_s is the skyrmion density, d_s is the skyrmion diameter, and w is the effective DW width. The resistance R is given by

$$R = \frac{1}{G} = \frac{1}{\frac{S}{\mathrm{RA}_P}(1 - \pi n_s d_s w) + \frac{S}{\mathrm{RA}_{AP}}(\pi n_s d_s w)} \tag{7}$$

and incorporates the resistance area products RA_P and RA_{AP} for parallel and anti-parallel states, respectively. This model helps understand skyrmion effects on TMR in MTJs, with parameters obtainable from TMR measurements and skyrmion imaging.

The role of temperature can be inferred from its impact on magnetization, which we recognize is crucial in shaping domain wall and skyrmion structures. Although temperature effects were not directly included in this manuscript, we acknowledge that free layer magnetization is sensitive to temperature, influencing both the texture and dynamics of domain walls and skyrmions (multimedia available online). Our results suggest that the core leaky-integrate functionality remains stable under varying thermal conditions. At higher temperatures, thermal fluctuations lead to observable skyrmion behavior changes, as skyrmion radius is temperature-dependent.[105] To counteract magnetization drops caused by elevated temperatures, using materials with higher exchange stiffness A and increased anisotropy K could enhance thermal stability. These adjustments provide more consistent magnetization dynamics, ensuring more stable skyrmion behavior during the writing and reading processes.

III. MODELLING MULTILAYER SPINTRONIC LEAKY INTEGRATE AND FIRE (LIF) SPIKING NEURONS

Leaky integrate-and-fire (LIF) neurons and synapses are fundamental components of spiking neural networks, which can consist of thousands or even millions of these units. To evaluate the feasibility of integrating these fabricated and proposed neurons at the circuit level, we have developed a compact behavioral LIF model. This model mimics the LIF characteristics through the output voltage read by the MTJ, which corresponds to domain wall (DW) propagation in response to current pulses. These pulses generate spikes via a comparator attached to the output terminal. The proposed model is assessed by the micromagnetic simulations, effectively capturing the LIF neuron characteristics.

A. Domain wall LIF neuron model

The proposed multilayer ferromagnetic DW-MTJ LIF neuron device is shown in Fig. 1. The energetics and dynamics of this device are detailed in Sec. III B. The correspondence between the DW-MTJ LIF model and bioplausible LIF characteristics is as follows: the net magnetization m of the free layer represents the LIF membrane potential $U(t)$, which is dependent on the DW position, as

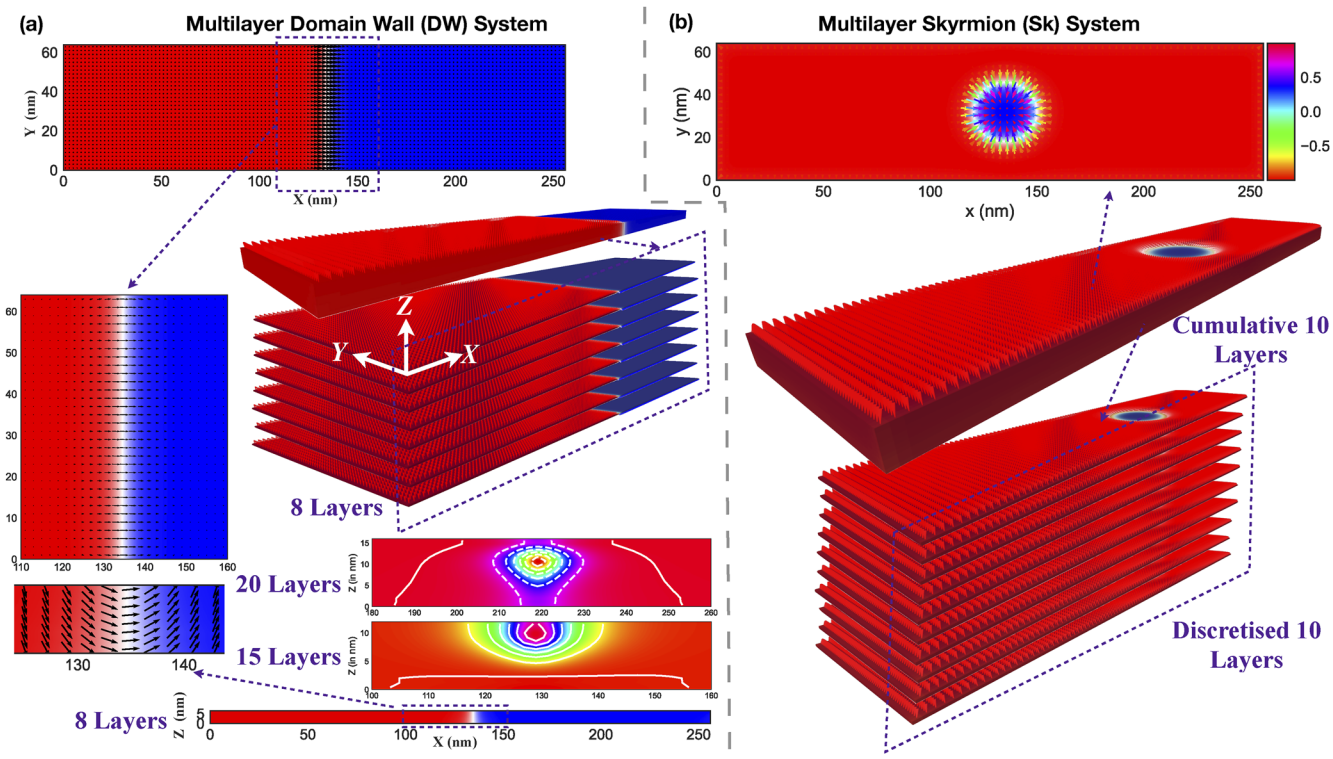

FIG. 5. Multilayer ferromagnetic stack decomposition analysis of (a) domain wall and (b) skyrmion.

shown in Fig. 5(a). As shown in magnetization evolution in Fig. 6(a), when current is applied, the DW propagates from one end to the other, continuously altering the free layer magnetization. In the absence of current, the increased demagnetization energy due to the DW shift in position, x, and boundary or edge repulsion creates a pinning/depinning force (multimedia available online). This force causes the DW to move back, reversing the magnetization and illustrating the leakage behavior of the LIF neuron. The propagation of DW in the presence of input current characterizes the integration [top three of Fig. 5(a)] and moving back in the absence (or reverse current) characterizes the leakage [bottom of Fig. 5(a)] behavior of the DW-LIF neuron. A video recording of DW's movement in the presence and absence of current pulse and their corresponding LIF evolution is shared in the supplementary material file (multimedia available online). A snapshot is shown in Fig. 7(b).

We obtain a differential equation corresponding to the evolution of net magnetization profile of DW. Since the net magnetization m depends upon the DW position x. We model the velocity ($dx/dt \propto dm/dt$) of the DW, which computes the magnetization time evolution as

$$\frac{dm}{dt} = \alpha \exp(-\beta m) + \gamma I(t), \tag{8}$$

which to the lowest order becomes

$$\frac{dm}{dt} = -\beta m + \alpha + \gamma I(t), \tag{9}$$

where m is the membrane potential, threshold = 5.8, $\alpha = -1 \times 10^7$, $\beta = -1.549$, $\gamma = 1.039 \times 10^{-3}$, $J = 1 \times 10^{11}$, and $dt = 2.3 \times 10^{-9}$. Using Eqs. (2) and (3), and with some algebraic modifications, the magnetization dynamics is translated into Hall voltage and or MTJ output neuron dynamics as

$$\frac{dU_{\text{mem}}}{dt} = \frac{1}{\tau} U_{\text{mem}} + \alpha + \gamma J(t). \tag{10}$$

The MTJ output voltage is further discretized, and the reset condition is added to the model as

$$U_{\text{mem}}(t + \Delta t) = U_{\text{mem}}(t) + dU_{\text{mem}}, \tag{11}$$

$$dU_{\text{mem}} = -U_{\text{mem}}(t)\frac{\Delta t}{\tau} + \{\gamma I(t) + \alpha\}\Delta t, \tag{12}$$

$$U_{\text{reset}} = \frac{\beta}{2.1} S U_{\text{th}}. \tag{13}$$

If the neuron generates a spike, indicated by an output spike through the comparator ($S = 1$),

$$S = \begin{cases} 1, & \text{if } U_{\text{mem}} > U_{\text{th}}, \\ 0, & \text{if } U_{\text{mem}} < U_{\text{th}}, \end{cases} \tag{14}$$

a reset MOSFET transistor permits a reset current pulse.

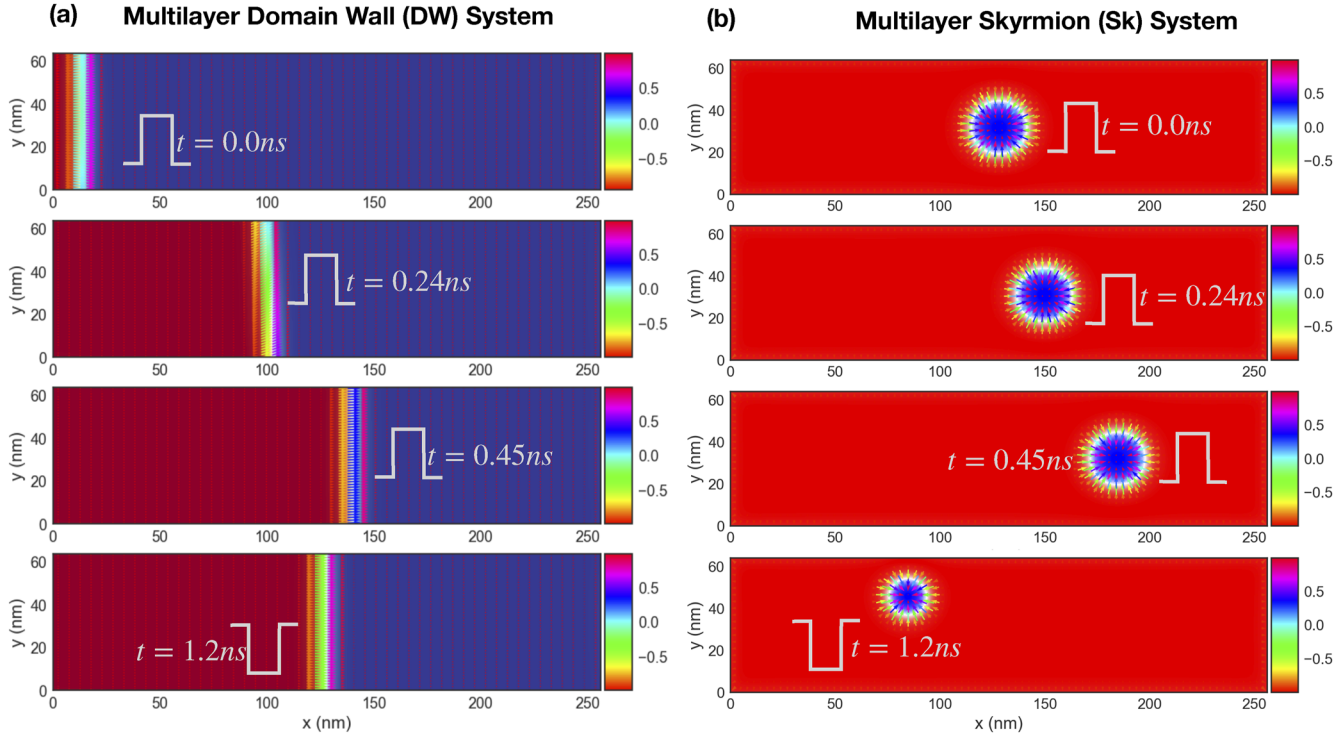

FIG. 6. Magnetization evolution throughout the LIF process. (a) Domain wall and (b) skyrmion.

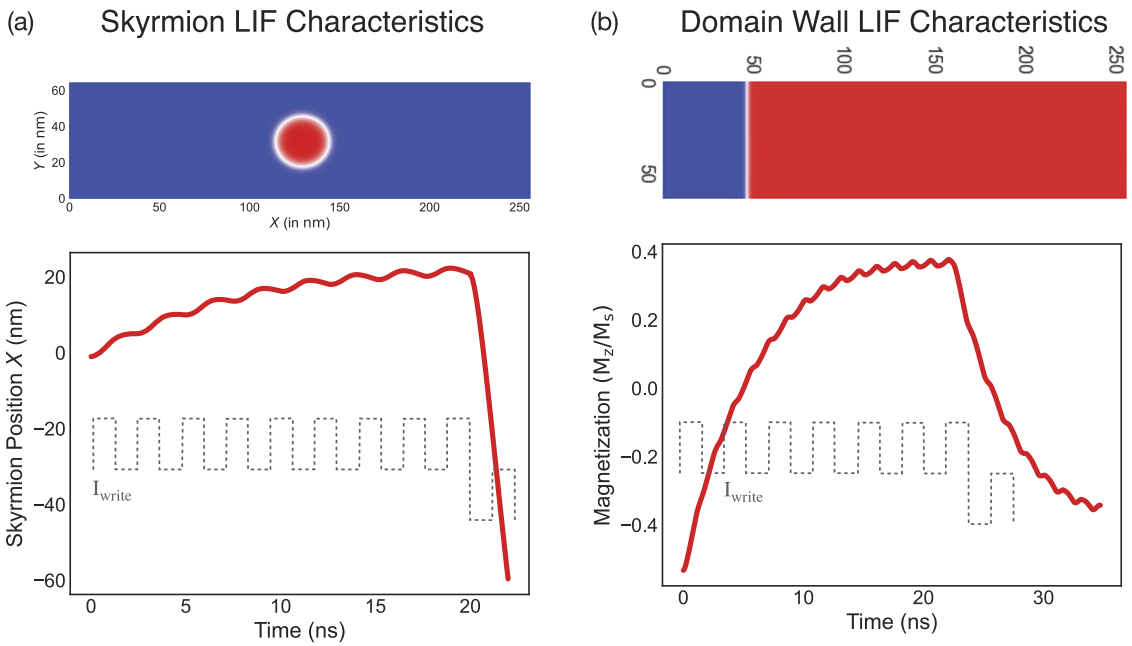

FIG. 7. Micromganetic simulation results depicting (a) skyrmion LIF behavior and (b) domain wall LIF behavior.

Figure 8(a) shows the characteristics of the LIF model under various current pulses. As shown, during the excitatory applied square current pulse period, the voltage increases due to integration and decreases due to leakage during the inhibitory pulse period. When the voltage reaches the threshold, the integration and leakage nearly cancel each other, causing the neuron to spike and triggering the reset mechanism. The dependency of the spike frequency of the DW-MTJ LIF model on the input current is shown in Fig. 9, demonstrating that as the current pulse increases, the spike frequency also rises.

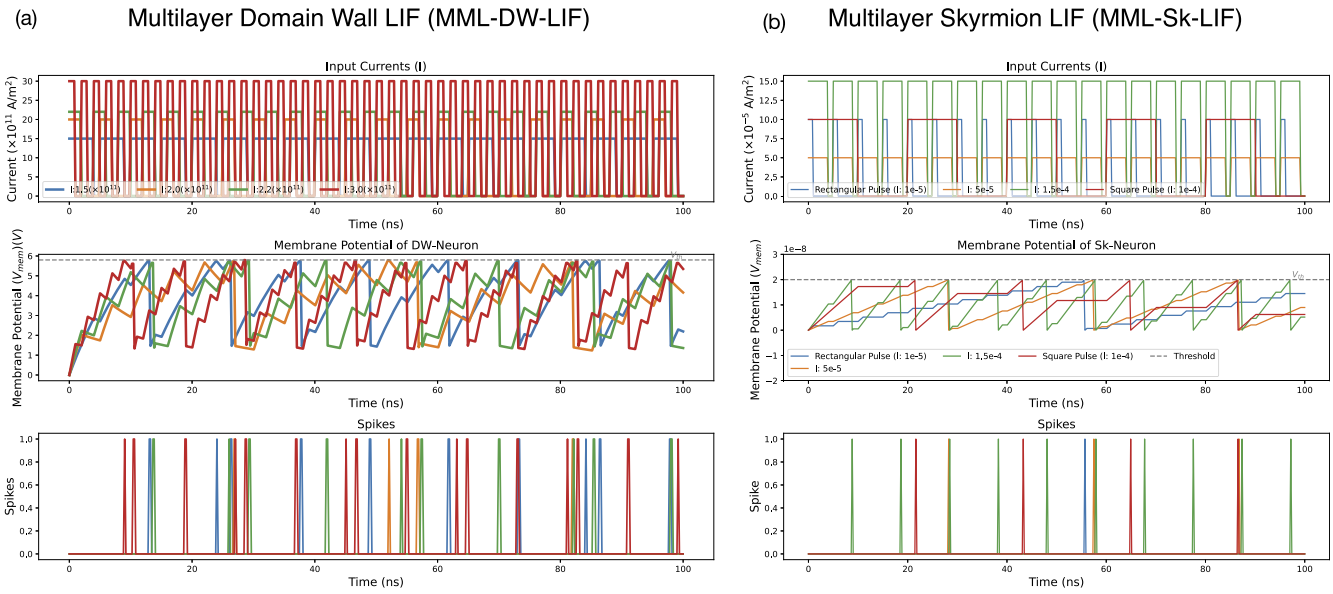

FIG. 8. Mathematical LIF Neuron model. (a) Domain wall (10) and (b) skyrmion (15).

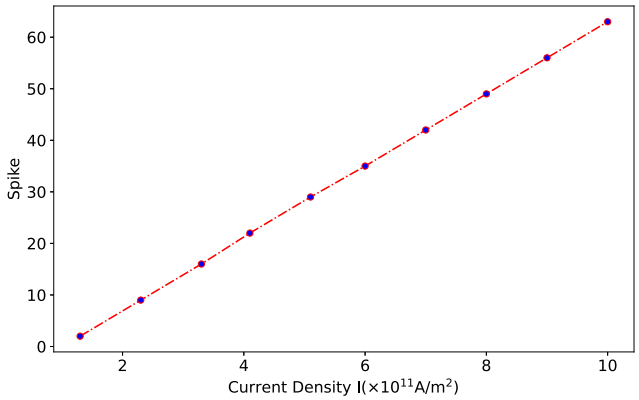

FIG. 9. Spike frequency response against current density.

B. Skyrmion LIF neuron model

Based on a similar idea and methodology, we have further simulated a multilayer skyrmion-based spintronic device [shown in Fig. 1(a) and simulated results shown in Fig. 5(b)] that emulates as a leaky integrate-and-fire (LIF) neuron in a spiking neural network by leveraging skyrmion motion for its functionality. The device structure comprises similar stacked nanotracks with additional chiral asymmetric DMI term, where the movement of skyrmions is initiated at one end and progresses toward the other transferring angular momentum adiabatically and non-adiabatically assisted by STT and SOT that results in the motion of skyrmion. The reading of the magnetization (membrane potential) is achieved using the tunneling magnetoresistance (TMR) effect via MTJ reading block. The reading of the neuron state variable *skyrmion position x*, as shown in Fig. 3(b), and magnetization in the case of the skyrmion LIF device is carried out by the tunneling magneto-resistance TMR effect via an MTJ reading block. As the skyrmion approaches the right end of the device, the demagnetization energy increases [in Fig. 3(c)], opposing the skyrmion movement. We put the reading MTJ near the right end of the nano tracks so that both state variables' integration in the presence of the current and leakage in the absence of the current is realized. A comparator connected to the MTJ output generates the magnified output spikes that propagate to the next layer. Ideally, the neuron should reset itself by moving the skyrmion to the left side of the nano track without any external stimulus, but it takes significant amount of time to realize the resetting of the membrane potential. To achieve this, a resetting current pulse is applied in the $-x$ direction once the membrane potential reaches U_{th} and the neuron fires. This activates the resetting MOSFET, returning the skyrmion to its initial position and resetting the membrane potential to U_{rest} on the left side of the nanotrack.

Thus, skyrmion's movement, influenced by STT and demagnetization forces, resembles the integration and leakage of membrane potential in biological neurons. Input current pulses drive the skyrmion, with subsequent reset pulses driving it back to its initial position upon reaching the threshold voltage. Overall, the device functions as a scalable LIF neuron, offering increased output signal and frequency response, essential for spiking neural networks. The skyrmion-based neuron model's response to input current and its neuronal behavior is shown in Fig. 7(a). A video recording of skyrmion's movement in the presence and absence of current pulse and their corresponding LIF evolution is shared in the supplementary material file [multimedia available online, mov (b)], a snapshot of which is shown in Fig. 7(a). We modeled the skyrmion position x as it moved across the nanotrack and obtained a differential equation by analyzing its velocity in the track,

$$\frac{dx}{dt} = k_1 x(t)^2 + k_2 x(t) + \gamma I(t), \tag{15}$$

where x imitates the membrane potential, threshold $x_{th} = 20 \times 10^{-9}$, $k_1 = -0.0026$, $k_2 = -0.0568$, $\gamma = 5.7529 \times 10^4$, $dt = 6 \times 10^{-11}$, $I(t) = 1 \times 10^{-4}$. In generic LIF neuronal equation, it can be written as

$$\tau \frac{dU_{\text{mem}}}{dt} = \tau \cdot k_1 U_{mem}^2 - \frac{1}{\tau} U_{mem} + R \cdot I(t), \tag{16}$$

where the decay term is $k_2 \cdot X = \frac{-V}{\tau}$ thus $k_2 = \frac{1}{\tau}$, the input current term $\gamma \cdot I(t) = R \cdot I(t)$ thus $\gamma = R$ and a quadratic non-linear term.

The MTJ output voltage is discretized, and the reset condition is added to the model as

$$U_{\text{mem}}(t+1) = U_{\text{mem}}(t) + dU_{\text{mem}}, \tag{17}$$

$$dU_{\text{mem}} = \Delta t\left(k_1 \Delta U_{\text{mem}}^2 + k_2 U_{\text{mem}} + k_3 I(t)\right). \tag{18}$$

If the neuron generates a spike, indicated by an output spike through the comparator ($S = 1$),

$$S = \begin{cases} 1, & \text{if } U_{\text{mem}} > U_{\text{th}}, \\ 0, & \text{if } U_{\text{mem}} < U_{\text{th}}, \end{cases} \tag{19}$$

a reset MOSFET transistor permits a reset current pulse in $-x$ direction that drives the skyrmion back to its original position.

Figure 8(b) shows the characteristics of the LIF model under various current pulse schemes. As shown, during the excitatory applied square current pulse period, the voltage increases due to integration and decreases due to leakage during the inhibitory pulse period. When the voltage reaches the threshold, the integration and leakage nearly cancel each other, causing the neuron to spike and triggering the reset mechanism.

IV. SNN IMPLEMENTATION

Furthermore, we implemented the proposed neuron models, both the domain wall and skyrmion in our spike neural network architecture based on snnTorch framework,[106] consisting of both the fully connected (FCSNN) layers as well as convoluted (CSNN) layers, with LIF neurons embedded at each node. We tested the performance of each model on classifying the MNIST handwritten digit dataset and Fashion F-MNIST classification using a modified spike-based backpropagation training approach.[107] For both the DW and Skyrmion LIF, the neural network architectures and training algorithms implemented were mostly similar as detailed. The FCSNN comprises three layers: 784 input neurons, 1000 neurons in the hidden layer, and 10 neurons in the output layer, as shown in Fig. 10(a).

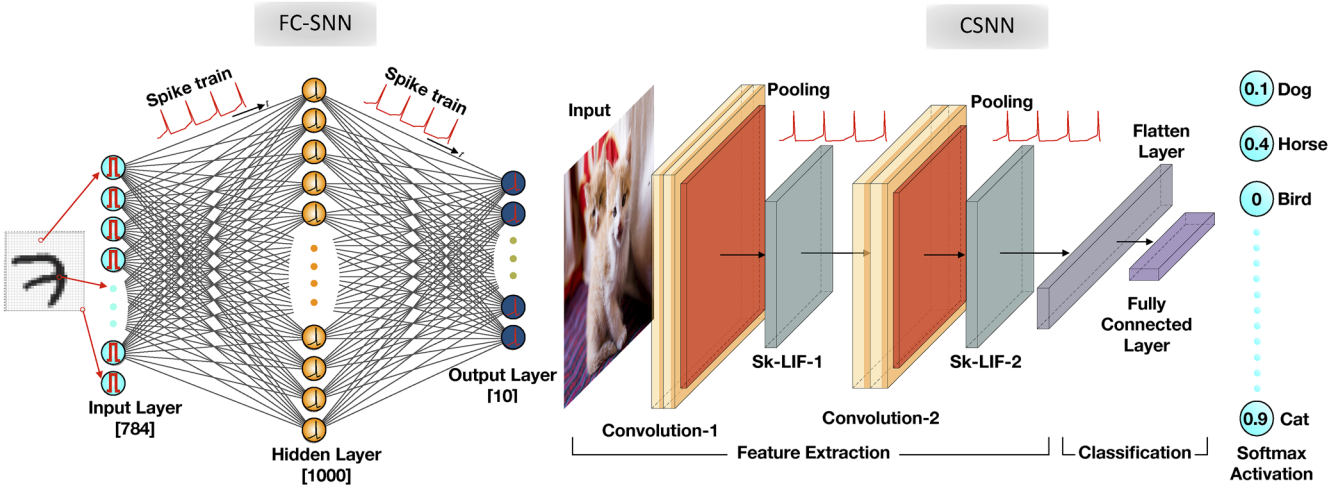

FIG. 10. Neural network architectures. (a) Three-layer fully connected spiking neural network (FC-SNN); (b) convolutional spiking neural network (CSNN) architecture-based on skyrmion neuron models.

In contrast, the CSNN includes two convolutional layers [Conv1 (1, 32, kernel = 5, padding = 5) and Conv2 (32, 64, kernel = 5, padding = 5), each followed by a MaxPool2d (kernel = 2, stride = 2) Pooling layers and the DW/Skyrmion LIF neuron are shown in Fig. 10(b)].

At $t = 0$, the membrane potential $U(t)$ represented by its variables $\tau, \gamma, \beta, \alpha, U, X, dt$, and the threshold values U_{th} initializes to its rest value. During each time step, the input flattens to maintain correct dimensional integrity. It then passes to the layers, where input spikes increase the membrane potential and generate spikes on reaching the threshold. We recorded these dynamics in the spike and membrane tensors across all layers, repeating this process for 60 steps. The system then returns the spike and membrane recordings to the network and CUDA device. As with the fully connected network, the input current and membrane potential pass through the network, and their dynamics are recorded over time. The training algorithm spans ten epochs at best for appending training and test loss assisted by membrane potential (FCSNN) and spike count (CSNN) calculated at each step using cross-entropy loss function. We have used the backpropagation algorithm [network architecture is shown in Fig. 11(a)] to train the network whose main aim is to reduce the error (loss) in a neural network. It does this by calculating the gradient of the loss with respect to each trainable parameter in the network. Using the chain rule involves working backward from the final layer to each weight,

$$\frac{\partial \mathcal{L}}{\partial W} = \frac{\partial \mathcal{L}}{\partial S} \underbrace{\frac{\partial S}{\partial U}}_{\{0,\infty\}} \frac{\partial U}{\partial I} \frac{\partial I}{\partial W}.$$

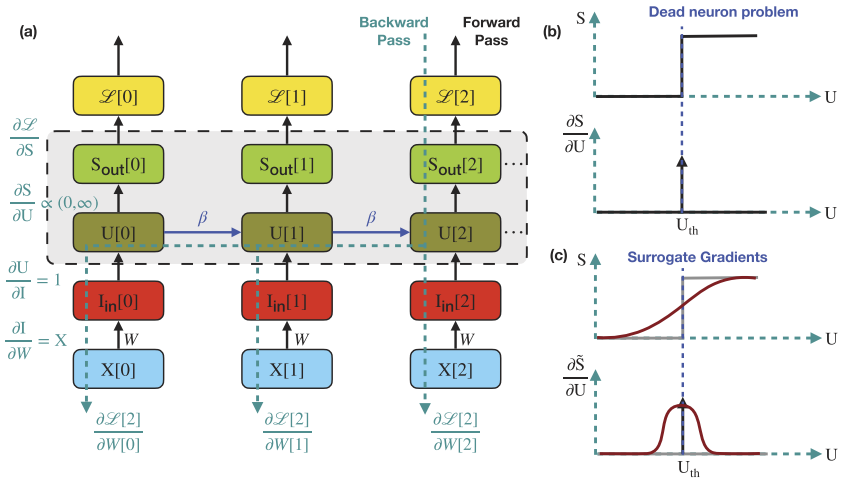

FIG. 11. (a) Backpropagation through time. (b) The dead neuron problem: the analytical solution that results in a gradient that does not enable learning. (c) Surrogate gradients: the spike generation function is approximated to a continuous function during the backward pass ("←" indicates function substitution), inspired from Ref. 106.

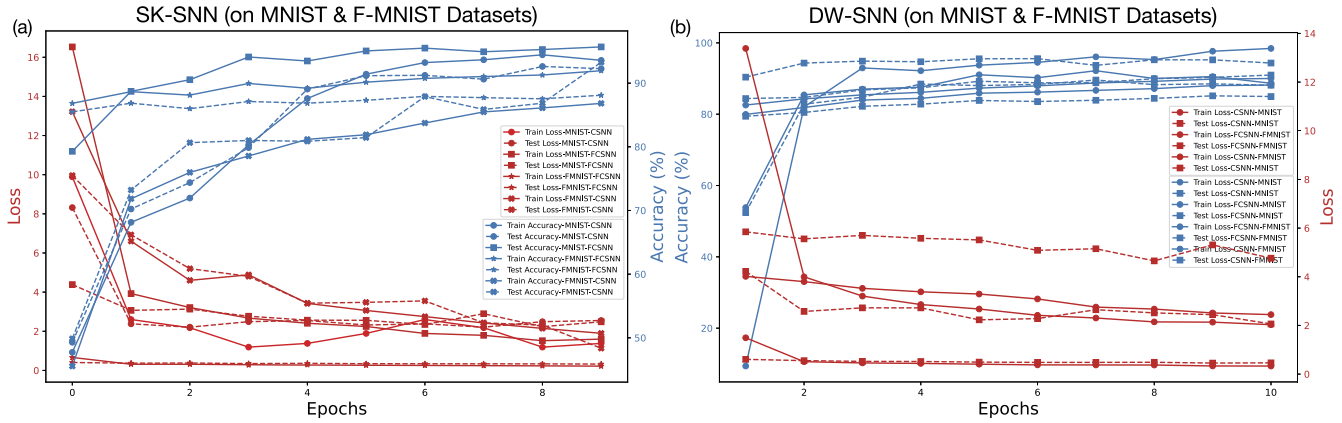

FIG. 12. Classification accuracy and loss on MNIST and FMNIST datatsets of (a) skyrmion LIF on FC-SNN and CSNN network; (b) domain wall LIF on FC-SNN and CSNN network.

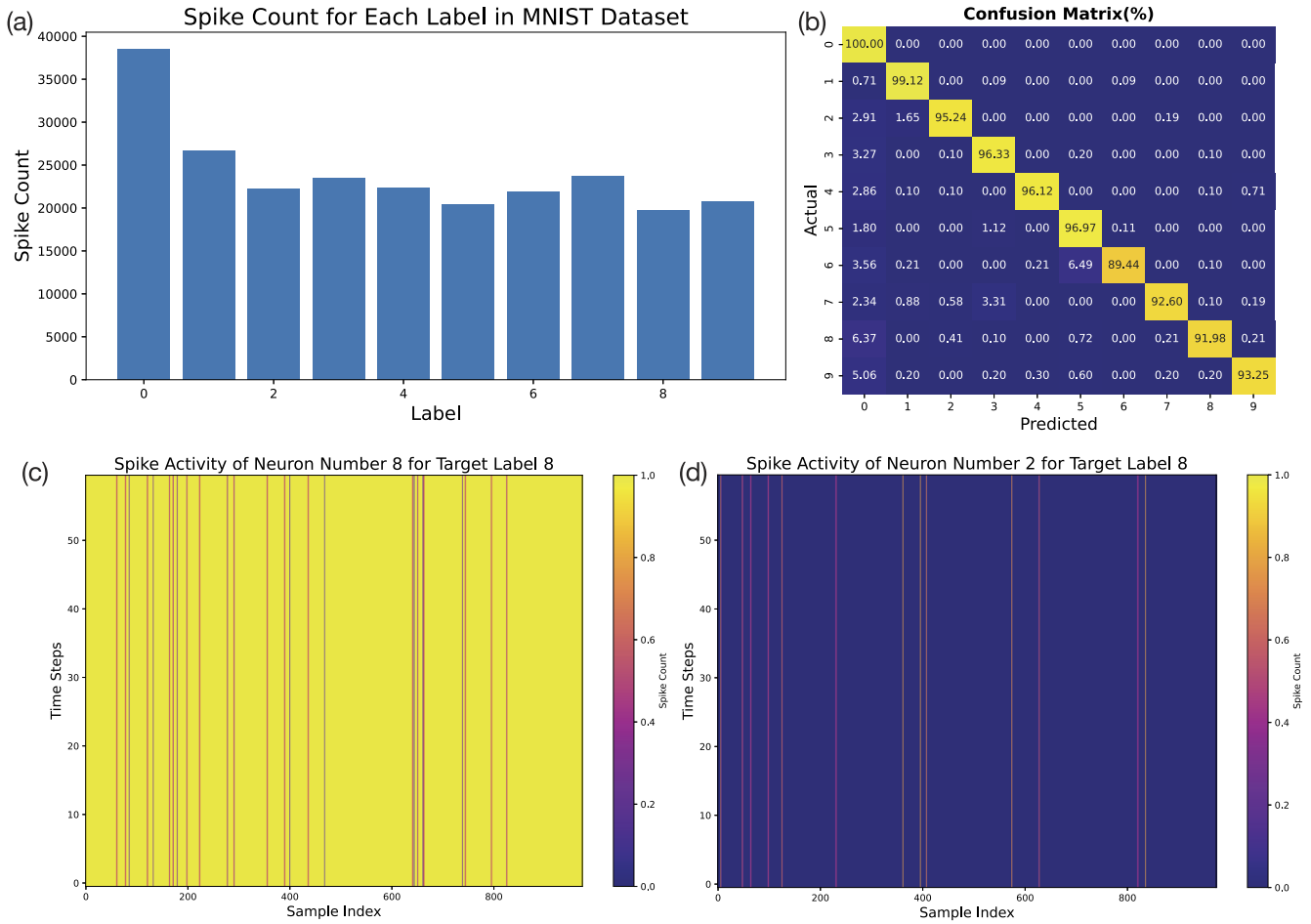

FIG. 13. SNN results. (a) Total measured spike count for each label (0–9), (b) confusion matrix plot for MNIST dataset, (c) heatmap of spike activity of final layer neuron no. 2 (Actual) when target is 2 constitutes the ACC 99.12%; (d) spike activity of final layer neuron no. (Actual) 2 when target is not 2 constitutes the ACC 0.01%.

ALGORITHM 1. Network architecture.

1: **Parameters:**
2: num_inputs ← 784
3: num_hidden ← 1000
4: num_outputs ← 10
5: num_steps ← 25
6: **Spiking Neuron Model:**
7: SKNeuron :
8: Parameters : i_{syn}, threshold, $p1, p2, \gamma, dt$
9: Forward pass :
10: $dv \leftarrow (p1 \cdot mem^2 + p2 \cdot mem + \gamma \cdot i_{\text{syn}}) \cdot dt$
11: Spike : $spk \leftarrow \text{Heaviside}(mem - \text{threshold})$
12: Reset : $mem \leftarrow mem + dv$
13: $mem \leftarrow \text{where}(spk == 1, mem - \text{threshold}, mem)$
14: **Network Class:**
15: Net :
16: Layers : fc1(num_inputs, num_hidden), lif1(), fc2(num_hidden, num_outputs), lif2()
17: Forward pass :
18: Initialize: $mem1, mem2$
19: **for** $step \in$ num_steps **do**
20: $cur1 \leftarrow fc1(x), spk1, mem1 \leftarrow lif1(cur1, mem1)$
21: $cur2 \leftarrow fc2(spk1), spk2, mem2 \leftarrow lif2(cur2, mem2)$
22: **end for**
23: Return: stack($spk2$), stack($mem2$)

ALGORITHM 2. Training procedure.

1: **Initialize Network:**
2: net ← Net().to(device)
3: **Loss and Optimizer:**
4: loss ← CrossEntropyLoss()
5: optimizer ← Adam(net.parameters(), lr = 0.005)
6: **Training Loop:**
7: **for** $epoch \in$ range(num_epochs) **do**
8: **for** $data, targets \in$ train_loader **do**
9: $data, targets \leftarrow data.to(device), targets.to(device)$
10: $spk\_rec, mem\_rec \leftarrow net(data.view(batch\_size, -1))$
11: loss_val ← $\sum_{step}^{num\_steps} \text{loss}(mem\_rec[step], targets)$
12: optimizer.zero_grad()
13: loss_val.backward()
14: optimizer.step()
15: **end for**
16: **end for**

Once these gradients are computed, they are used to adjust the weights to minimize the error. However, in training spike neural networks (SNNs), one major problem occurs when the gradient is zero, which means that the weights will not be updated since the spikes are in the form of 0s and 1s so the derivative turns out to be non-differentiable in the term $\partial S/\partial U \in \{0, \infty\}$. This issue, known as the "dead neuron" problem, arises when neurons fail to fire, making their gradients zero and preventing them from learning,

$$S = \begin{cases} 1, & U > U_{\text{th}}, \\ 0, & U < U_{\text{th}}. \end{cases} \tag{20}$$

To address the above-mentioned issues, the surrogate gradient approach is utilized by substituting non-differentiable spike functions with continuous functions during the backward pass while keeping the Heaviside function during the forward pass, as shown in Fig. 11(b). For example, instead of using the Heaviside step function (which is non-differentiable) Eqn. (20), a continuous function $\tilde{S}$ such as the sigmoid/fastsigmoid/arctan function is used. This allows the error to propagate even if a neuron does not fire, ensuring that all neurons, including inactive ones, receive appropriate gradient signals during training. However, weight updates still depend on actual spiking events to ensure meaningful learning,

$$S \sim \frac{1}{\pi} \arctan(\pi U), \tag{21}$$

$$\frac{\partial S}{\partial U} = \frac{1}{\pi} \frac{1}{1 + (\pi U)^2}. \tag{22}$$

For our training network, the backpropagation through time (BPTT) algorithm was assisted by the sigmoid function in Eq. (20) that helps compute gradients over time, and an optimizer such as Adam (with a learning rate of 0.0009) is used to update the weights and improve accuracy. Following training, we tested our devices and models with test data, analyzing accuracy with increasing iterations and epochs, and compared results with the snntorch's ideal LIF neuron snnLeaky as a benchmark. The proposed neuron models achieved results comparable with the ideal SnnLeaky neuron model. Both the DW-based and Skyrmion-based SNN architectures (FCSNN and CSNN) have achieved over 90% accuracy on MNIST and FMNIST datasets shown in Fig. 12, demonstrating the effectiveness of these methods. The spike activity of each neuron is traced individually [Fig. 13(a)], which is shown in Fig. 13(c), where neuron No. 2 spikes all the time when target is set 2 while spikes rarely [Fig. 13(d)] when spike is not 2. This correlation between the actual and predicted digits is depicted using a confusion matrix in Fig. 13(c). These accuracy results, when added to the low latency neuron metrics and low writing energy requirements, underscore the viability of the proposed neuron models for large-scale energy-efficient neuromorphic computing applications.

A. SNN algorithms

The full algorithm developed for the SNN dataset classification is presented in the supplementary material file. However, the network and training algorithms are as follows (Algorithm 1 and 2).

V. CONCLUSION

In this paper, we propose spintronic domain wall and skyrmion based multilayer ferromagnetic LIFneuron device concepts, along with their mathematical models, and demonstrate their integration into bio-realistic, energy-efficient spiking neural networks (SNNs). LIF behavior is achieved through a combination of spin-transfer torque (STT), spin–orbit torque (SOT), various energy interactions, and input current pulse schemes. The advantages of the proposed device concept include its multilayer ferromagnetic structure, which

is highly resilient and stable, allowing domain walls and skyrmions to be hosted at ultra-small sizes, thereby enabling high-density integration, scalability, and efficient latency. The integration and leak functionality of the neuron is achieved by modulating the demagnetizing energy. We demonstrate the spintronic mem-transistor-like behavior, which provides dual tunability and versatility in device operation. Using micromagnetic simulations, we illustrate the device's functionality at low spike latency and its LIF characteristics for applied input pulses. We integrated the neuron models into fully connected and convolutional SNN architectures using a modified spike-based backpropagation technique to perform image recognition tasks. We achieved an accuracy of 98% when classifying the MNIST handwritten digits dataset and 95% when classifying the FMNIST dataset. With such strong metrics, the proposed neurons and SNN schemes show excellent prospects for spiking neural network applications and neuromorphic computing in general.

SUPPLEMENTARY MATERIAL

The supplementary material is available from the AIP Online Library or the author.

ACKNOWLEDGMENTS

This work acknowledges the support from the University of Delhi, IN.

AUTHOR DECLARATIONS

Conflict of Interest

The authors have no conflicts to disclose.

Author Contributions

Kishan K. Mishra: Writing – original draft (lead).

DATA AVAILABILITY

The code used to generate the desirable result is available from the corresponding author upon reasonable request.

APPENDIX A: BIOLOGICAL, ARTIFICIAL AND SPIKING NEURON

Neurons, whether biological, artificial, or spiking, are the fundamental units of computation in their respective systems, each with distinct principles, characteristics, and efficiencies. *Biological neurons* operate based on electrochemical processes: they receive inputs through dendrites, process them in the soma, and transmit outputs via action potentials along the axon to synapses shown in Fig. 14(a). The biorealistic model Hodgkin–Huxley model[91,108,109] describes the ionic currents through the neuron membrane using differential equations, capturing the dynamics of voltage-gated ion channels (e.g.,

$$I = C_m \frac{dU_{\text{mem}}}{dt} + I_{Na} + I_K + I_L,$$

where I is the total membrane current, C_m is the membrane capacitance, and U_{mem} is the membrane potential). It exhibits firing at a constant rate for a constant input, called tonic spiking and allows for spike-time dependent plasticity (STDP), as shown in Fig. 14(b).[109]

Artificial neurons, on the other hand, abstract this process through mathematical models in artificial neural networks (ANNs).[110] These neurons compute a weighted sum of inputs, pass it through an activation function f (e.g., sigmoid, ReLU), and produce an output,

$$y = f\left(\sum w_i x_i + b\right),$$

where w_i are the weights, x_i are the inputs, and b is the bias.

Spiking neurons, akin to the biological counterparts, communicate via discrete spikes rather than continuous signals. The dynamics of spiking neurons can be described by models such as the leaky integrate-and-fire (LIF) model, where the membrane potential $U_{\text{mem}}(t)$ evolves according[93] to

$$\tau_m \frac{dU_{\text{mem}}(t)}{dt} = -U_{\text{mem}}(t) + RI(t),$$

with τ_m being the membrane time constant and R being the resistance. When $U_{\text{mem}}(t)$ reaches a threshold, a spike is emitted, and $U_{\text{mem}}(t)$ is reset. Biological neurons are highly efficient in energy consumption and adaptability but are slower compared to artificial neurons, which excel in speed and scalability but consume significant power and lack biological complexity. Spiking neurons offer a middle ground, mimicking biological neurons' efficiency and temporal dynamics while maintaining computational advantages over traditional ANNs. Biological neurons leverage chemical gradients for low-power operation, artificial neurons benefit from parallelized hardware implementations, and spiking neurons utilize sparse, event-driven processing, optimizing power and computational resources in neuromorphic hardware. Both ANNs and spiking neural networks (SNNs) can model similar network topologies, but they differ in neuron models: ANNs use artificial neurons with weighted sum inputs and non-linear functions such as sigmoid or ReLU, whereas SNNs use spiking neurons that affect a neuron's membrane potential, $U_{\text{mem}}(t)$. Neuromorphic engineering[111] aims to replicate the brain's computational principles to reduce energy costs in AI systems, comprising three main components: neuromorphic sensors inspired by biological sensors, neuromorphic algorithms (SNNs), and specialized hardware for power-efficient execution. These systems leverage sparse activations and low-precision parameters to accelerate neuromorphic workloads, resulting in significant power and latency gains.[112] By emulating the brain's efficiency, neuromorphic systems aim to bridge the gap between current and future intelligent systems. The complexities of training brain-inspired neuromorphic algorithms underscore the importance of extracting learning algorithms from the brain to improve AI. While SNNs can be optimized with existing tools, the unique nature of biologically inspired neural networks warrants further exploration. Two fundamental dynamics constituting the SNN are neurons and synapses. Pre-neuron transmits voltage spikes $\sum_f \delta(t - t_f)$ to post-neuron through synapses. The synapses model the generated spikes as

$$\tau_{post} \frac{dI_{post}}{dt} = -I_{post} + w \sum_f \delta(t - t_f),$$

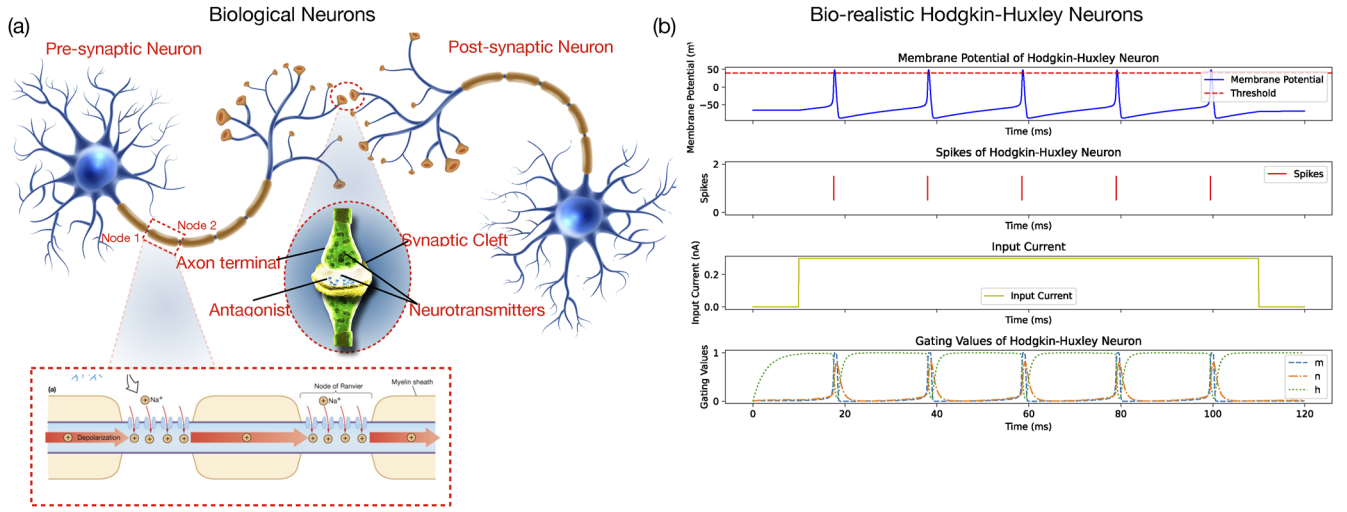

FIG. 14. (a) Schematic of biological neuron, synaptic connections (dotted encircled), and ion channels (dotted square box); (b) mathematical response of the Huxley–Hodgkin (H–H) neuron model.

where I_{post} is the synaptic current modulated by synaptic conductance (weight) w over spikes and decays with time constant τ_{post}. Once post-neuron receives the synaptic current, its dynamics are governed by

$$\tau \frac{dU_{\text{mem}}}{dt} = -U_{\text{mem}} + R_{\text{mem}} \sum I_{post,i},$$

where U_{mem} characterizes the membrane potential, R_{mem} is membrane resistance, $I_{post,i}$ is the post-synaptic current input from the ith neuron, and τ is the membrane time constant. When the membrane potential reaches a certain threshold, U_{th}, the neuron emits a spike. Inputs to neurons are typically short bursts of electrical activity (spikes). Because these input spikes rarely arrive simultaneously, the membrane potential exhibits temporal dynamics, sustaining it over time. This concept was first quantified in 1907 by Louis Lapicque, who likened a spiking neuron to a low-pass filter circuit composed of a resistor (R) and a capacitor (C), which was later named the leaky integrate-and-fire (LIF) neuron model.

To integrate this time-dependent behavior into a sequence-based neural network, the forward Euler method is used to approximate the neuron's membrane potential, $U_{\text{mem}}[t]$,

$$U_{\text{mem}}[t] = \beta U_{\text{mem}}[t-1] + (1-\beta) I_{\text{in}}[t]. \tag{A1}$$

Here, time is discretized, and $\beta = e^{-1/\tau}$ represents the decay rate or inverse time constant of $U_{\text{mem}}[t]$. In deep learning, input weighting factors are learnable parameters, so the coefficient of input current $(1-\beta)$ can be incorporated into a learnable weight W. This simplifies the input current to $I_{\text{in}}[t] = WX[t]$, isolating the effect of β on the input $X[t]$. Including the effects of spiking and membrane potential reset, the model becomes

$$U_{\text{mem}}[t] = \beta U_{\text{mem}}[t-1] + WX[t] - S_{\text{out}}[t-1] U_{\text{th}}, \tag{A2}$$

where $S_{\text{out}}[t] \in \{0, 1\}$ is the output spike. If a spike is generated (i.e., $S_{\text{out}} = 1$), the reset term subtracts θ from the membrane potential. Otherwise, the reset term has no effect. A spike is generated if the membrane potential exceeds the threshold,

$$S_{\text{out}}[t] = \begin{cases} 1, & \text{if } U_{\text{mem}}[t] > U_{\text{th}}, \\ 0, & \text{otherwise.} \end{cases} \tag{A3}$$

The ideal leaky integrate-and-fire (LIF) neuron model is implemented in the snnTorch library[106,113] as `Snn.Leaky`. This implementation captures the described dynamics, enabling the simulation and analysis of SNNs within the framework.

Now comes the part when input data are being encoded and sent to the network. For SNNs, the input data do not have to be encoded into spikes; continuous values as input data are also acceptable. For example, an "image" is "static data" that can be treated as a direct current (DC) input with the same features passed to the input layer of the SNN at every time step. There are three main mechanisms to encode the input data.

1. **Rate coding** converts input intensity into a firing rate or spike count and chooses the output neuron with the highest firing rate, or spike count, as the predicted class.
2. **Latency (or temporal) coding** converts input intensity to a spike time and chooses the output neuron that fires first as the predicted class.
3. **Delta modulation** converts a temporal change of input intensity into spikes, and otherwise remains silent and applies the above-mentioned coding schemes (typically a rate code) with multiple neurons per class.

APPENDIX B: SOLITON DYNAMICS AND MICROMAGNETIC SIMULATIONS

Numerous literary studies have extensively delved into fundamental elementary processes, such as nucleation, annihilation, reading, writing, manipulation, and dynamics, concerning skyrmions

and domain walls across various nanostructures.[36,65] In this discussion, we will focus on the essential aspects relevant to our topic without delving into exhaustive details. The nucleation of solitons, including both domain walls (DWs) and skyrmions, can be achieved by applying a spin current ("write current" between T-1 and T-2, 5–10 mA) in the proposed device structure. Once nucleated, the DW or skyrmion can be displaced by a charge current passing through the heavy metal (HM). The motion of these solitons can be controlled by a current either in-plane (CIP) or perpendicular to the plane (CPP). The dynamics of skyrmion CIP and CPP have been extensively studied in the review paper.[65]

The dynamics of skyrmions can be described using the Thiele equation for the velocity vector $\boldsymbol{v} = (v_x, v_y)$,

$$\mathscr{G} \times \boldsymbol{v} - \alpha[\mathscr{D}]\boldsymbol{v} + \mathscr{F} + \mathscr{F}^{\text{ext}} = 0, \tag{B1}$$

with

$$\begin{aligned} G &= -\frac{M_s t_{\text{FM}}}{\gamma} \iint \left\{ \left(\frac{\partial \boldsymbol{m}}{\partial x} \times \frac{\partial \boldsymbol{m}}{\partial y} \right) \cdot \boldsymbol{m} \right\} dx\, dy, \\ [\mathscr{D}] &= \begin{bmatrix} D_{xx} D_{xy} \\ D_{yx} D_{yy} \end{bmatrix}, \quad D_{ij} = \frac{M_s t_{\text{FM}}}{\gamma} \iint \left\{ \frac{\partial \boldsymbol{m}}{\partial i} \cdot \frac{\partial \boldsymbol{m}}{\partial j} \right\} dx\, dy, \\ F_{x,y} &= \frac{\mu_0 M_s t_{\text{FM}}}{\gamma} \iint \left\{ (\boldsymbol{m} \times \boldsymbol{\tau}) \cdot \frac{\partial \boldsymbol{m}}{\partial x, y} \right\} dx\, dy, \\ \mathscr{F}^{\text{ext}} &= -\int \frac{\delta \mathscr{U}}{\delta \boldsymbol{m}} \cdot \frac{\partial \boldsymbol{m}}{\partial x, y} dx\, dy = -\frac{\partial \mathscr{U}}{\partial x, y} = -\nabla \mathscr{U}(\boldsymbol{r}), \end{aligned} \tag{B2}$$

where $\mathscr{G} = G\hat{z}$ is the gyrovector, $\mathscr{D}$ is the dissipation matrix, and $\mathscr{F} = (F_x, F_y)$ represents the force on the skyrmion magnetization due to the spin–orbit torque (SOT) $\boldsymbol{\tau}$.

SOT induces magnetization dynamics in ferromagnetic (FM) layers through a vertical pure spin-current $\boldsymbol{j}_s$ injected from other layers, typically HM layers. This interaction is described by the modified Landau–Lifshitz–Gilbert (LLG) equation,

$$\begin{aligned} \frac{d\boldsymbol{m}}{dt} &= -\gamma \mu_0 \boldsymbol{m} \times \mathbf{H}_{\text{eff}} + \alpha \left(\boldsymbol{m} \times \frac{d\boldsymbol{m}}{dt} \right) \\ &\quad - \gamma \frac{\hbar}{2e} \frac{j}{\mu_0 M_s t_{\text{FM}}} \theta_{\text{eff}} \boldsymbol{m} \times (\boldsymbol{m} \times \hat{\mathbf{s}}), \end{aligned} \tag{B3}$$

where γ is the gyromagnetic ratio, $\mathbf{H}_{\text{eff}}$ is the effective field, and α is the Gilbert damping parameter. Micromagnetic simulations using MuMax[79] incorporate this equation, with SOT added as modified spin-transfer torque (STT),

$$\boldsymbol{\tau}_{\text{SOT}} = -\frac{\gamma}{1+\alpha^2} a_J [(1 + \xi\alpha)\boldsymbol{m} \times (\boldsymbol{m} \times \boldsymbol{p}) + (\xi - \alpha)(\boldsymbol{m} \times \boldsymbol{p})], \tag{B4}$$

$$a_J = \left| \frac{\hbar}{2M_s e \mu_0} \frac{\theta_{\text{SH}} j}{d} \right|, \quad \mathbf{p} = \text{sign}(\theta_{\text{SH}}) \mathbf{j} \times \mathbf{n}, \tag{B5}$$

where θ_{SH} is the spin Hall coefficient, j is the current density, and d is the free layer thickness. The resistance of the skyrmion magnetic tunnel junction (MTJ) synapse is computed using the magnetization profile of the free layer,[97]

$$R_{\text{syn}} = \frac{V_{\text{syn}}}{I_{\text{syn}}}. \tag{B6}$$

The effective magnetic field $\boldsymbol{H}_{\text{eff}}$ is defined as

$$\boldsymbol{H}_{\text{eff}} = \frac{-1}{\mu_0 M_s} \frac{\delta \boldsymbol{E}}{\delta \boldsymbol{m}}. \tag{B7}$$

The total magnetic energy $\boldsymbol{E}(\boldsymbol{m})$ of the free layer includes exchange, uniaxial anisotropy, Zeeman energy, demagnetization, and DMI energies,[36,38,115]

$$\begin{aligned} \boldsymbol{E}(\boldsymbol{m}) = \int_V \Big[& A(\nabla \boldsymbol{m})^2 - \mu_0 \boldsymbol{m} \cdot \boldsymbol{H}_{\text{ext}} - \frac{\mu_0}{2} \boldsymbol{m} \cdot \boldsymbol{H}_d \\ & - K_u (\hat{u} \cdot \boldsymbol{m})^2 + \varepsilon_{\text{DM}} \Big] dv, \end{aligned}$$

where A is the exchange stiffness, μ_0 is the permeability, K_u is the anisotropy energy density, H_d is the demagnetization field, and H_{ext} is the external field. The DMI energy density $\boldsymbol{\varepsilon}_{\text{DM}}$ is computed as

$$\boldsymbol{\varepsilon}_{\text{DM}} = D[m_z(\nabla \cdot \boldsymbol{m}) - (\boldsymbol{m} \cdot \nabla) \cdot \boldsymbol{m}]. \tag{B8}$$

Solving the Euler equation yields the domain wall width (δ) and domain wall energy with DMI (σ),[116]

$$\delta = \pi\Delta = \pi\sqrt{\mathcal{A}/\mathcal{K}_{\text{eff}}}, \tag{B9}$$

$$\sigma = 4\sqrt{\mathcal{A}\mathcal{K}_{\text{eff}}} \mp \pi\mathcal{D}, \tag{B10}$$

where $\Delta = \mathcal{A}/\mathcal{K}_{\text{eff}}$ is the Bloch wall width parameter.

Magnetic skyrmions are characterized by their topological or skyrmion number Q,

$$Q = \frac{1}{4\pi} \iint \mathbf{m} \cdot \left(\frac{\partial \mathbf{m}}{\partial x} \times \frac{\partial \mathbf{m}}{\partial y} \right) dx\, dy. \tag{B11}$$

The spins projected on the XY-plane and the normalized magnetization vector $\boldsymbol{m}$ can be expressed using the radial function θ, vorticity Q_v, and helicity Q_h,

$$m(r) = [\sin(\theta)\cos(Q_v\varphi + Q_h), \sin(\theta)\sin(Q_v\varphi + Q_h), \cos(\theta)]. \tag{B12}$$

The vorticity number is related to the skyrmion number as follows:

$$Q = \frac{Q_v}{2} \left[\lim_{r \to \infty} \cos(\theta(r)) - \cos(\theta(0)) \right]. \tag{B13}$$

Skyrmions in motion are subject to the Magnus force and input spike currents from presynaptic neurons, which can lead to edge annihilation if the current density exceeds a critical threshold. The skyrmion Hall effect limits the applicability of skyrmion motion. Reduction in skyrmion size along the edge can cause deceleration and potential temperature-activated annihilation. Multilayer skyrmions, as discussed in Ref. 87, provide enhanced stability against thermal fluctuations and external perturbations compared to single-layer skyrmions. They can be manipulated at smaller sizes, offering better scalability for magnetic memory technologies. The motion of multilayer skyrmions has been studied for achieving higher velocities and reduced sizes in a structure of dimensions 256×64 nm^2. Upon continuous input current, skyrmions reach a threshold and fire an output signal after a certain time (e.g., $t = 12$ ns).

REFERENCES

[1] S. K. Sood and Pooja, IEEE Trans. Eng. Manage. **71**, 6662 (2024).
[2] C. Mead, Proc. IEEE **78**, 1629 (1990).
[3] M. Kjaergaard, M. E. Schwartz, J. Braumüller, P. Krantz, J. I.-J. Wang, S. Gustavsson, and W. D. Oliver, Annu. Rev. Condens. Matter Phys. **11**, 369 (2020).
[4] R. P. Feynman, *Feynman and Computation* (CRC Press, 2018), pp. 133–153.
[5] D. Deutsch and A. Ekert, Phys. World **11**, 47 (1998).
[6] E. Chicca, F. Stefanini, C. Bartolozzi, and G. Indiveri, Proc. IEEE **102**, 1367 (2014).
[7] D. Marković, A. Mizrahi, D. Querlioz, and J. Grollier, Nat. Rev. Phys. **2**, 499 (2020).
[8] K. Roy, A. Jaiswal, and P. Panda, Nature **575**, 607 (2019).
[9] C. D. Schuman, S. R. Kulkarni, M. Parsa, J. P. Mitchell, P. Date, and B. Kay, Nat. Comput. Sci. **2**, 10 (2022).
[10] W. Maass, Neural Networks **10**, 1659 (1997).
[11] M. Bouvier, A. Valentian, T. Mesquida, F. Rummens, M. Reyboz, E. Vianello, and E. Beigne, ACM J. Emerging Technol. Comput. Syst. **15**, 1 (2019).
[12] P. A. Merolla, J. V. Arthur, R. Alvarez-Icaza, A. S. Cassidy, J. Sawada, F. Akopyan, B. L. Jackson, N. Imam, C. Guo, Y. Nakamura *et al.*, Science **345**, 668 (2014).
[13] M. Davies, N. Srinivasa, T.-H. Lin, G. Chinya, Y. Cao, S. H. Choday, G. Dimou, P. Joshi, N. Imam, S. Jain *et al.*, IEEE Micro **38**, 82 (2018).
[14] A. Sengupta, Y. Ye, R. Wang, C. Liu, and K. Roy, Front. Neurosci. **13**, 95 (2019).
[15] S. Ghosh-Dastidar and H. Adeli, Int. J. Neural Syst. **19**, 295–308 (2009).
[16] K. M. Song, J.-S. Jeong, B. Pan, X. Zhang, J. Xia, S. Cha, T.-E. Park, K. Kim, S. Finizio, J. Raabe *et al.*, Nat. Electron. **3**, 148 (2020).
[17] Z. He and D. Fan, in *Design, Automation and Test in Europe Conference and Exhibition (DATE)* (IEEE, 2017), pp. 350–355.
[18] J. J. Wade, L. J. McDaid, J. A. Santos, and H. M. Sayers, IEEE Trans. Neural Networks **21**, 1817 (2010).
[19] M.-C. Chen, A. Sengupta, and K. Roy, IEEE Trans. Magn. **54**, 1 (2018).
[20] C. Havenstein, D. Thomas, and S. Chandrasekaran, SMU Data Sci. Rev. **1**(4), 11 (2018), see https://scholar.smu.edu/datasciencereview/vol1/iss4/11.
[21] S. Furber, J. Neural Eng. **13**, 051001 (2016).
[22] A. Beck, J. Bednorz, C. Gerber, C. Rossel, and D. Widmer, Appl. Phys. Lett. **77**, 139 (2000).
[23] J. Feldmann, N. Youngblood, C. D. Wright, H. Bhaskaran, and W. H. Pernice, Nature **569**, 208 (2019).
[24] D. Kuzum, R. G. Jeyasingh, B. Lee, and H.-S. P. Wong, Nano Lett. **12**, 2179 (2012).
[25] H. Mulaosmanovic, E. Chicca, M. Bertele, T. Mikolajick, and S. Slesazeck, Nanoscale **10**, 21755 (2018).
[26] A. Sengupta, P. Panda, P. Wijesinghe, Y. Kim, and K. Roy, Sci. Rep. **6**, 30039 (2016).
[27] I. Žutić, J. Fabian, and S. D. Sarma, Rev. Mod. Phys. **76**, 323 (2004).
[28] J. Torrejon, M. Riou, F. A. Araujo, S. Tsunegi, G. Khalsa, D. Querlioz, P. Bortolotti, V. Cros, K. Yakushiji, A. Fukushima *et al.*, Nature **547**, 428 (2017).
[29] J. Grollier, D. Querlioz, K. Camsari, K. Everschor-Sitte, S. Fukami, and M. D. Stiles, Nat. Electron. **3**, 360 (2020).
[30] B. Dieny, I. L. Prejbeanu, K. Garello, P. Gambardella, P. Freitas, R. Lehndorff, W. Raberg, U. Ebels, S. O. Demokritov, J. Akerman *et al.*, Nat. Electron. **3**, 446 (2020).
[31] G. Finocchio, M. Di Ventra, K. Y. Camsari, K. Everschor-Sitte, P. Khalili Amiri, and Z. Zeng, J. Magn. Magn. Mater. **521**, 167506 (2021).
[32] S. Chowdhury, A. Grimaldi, N. A. Aadit, S. Niazi, M. Mohseni, S. Kanai, H. Ohno, S. Fukami, L. Theogarajan, G. Finocchio *et al.*, IEEE J. Explor. Solid-State Comput. Devices Circuits **9**, 1 (2023).
[33] J. Deng, V. P. K. Miriyala, Z. Zhu, X. Fong, and G. Liang, IEEE Electron Device Lett. **41**, 1102 (2020).
[34] J.-Y. Lee, K.-S. Lee, S. Choi, K. Y. Guslienko, and S.-K. Kim, Phys. Rev. B **76**, 184408 (2007).
[35] A. M. Kosevich, B. Ivanov, and A. S. Kovalev, Phys. Rep. **194**, 117 (1990).
[36] A. Fert, V. Cros, and J. Sampaio, Nat. Nanotechnol. **8**, 152 (2013).
[37] J. Sampaio, V. Cros, S. Rohart, A. Thiaville, and A. Fert, Nat. Nanotechnol. **8**, 839 (2013).
[38] K. Everschor-Sitte, J. Masell, R. M. Reeve, and M. Kläui, J. Appl. Phys. **124**, 240901 (2018).
[39] Y. Liu, W. Hou, X. Han, and J. Zang, Phys. Rev. Lett. **124**, 127204 (2020).
[40] B. Sutton, K. Y. Camsari, B. Behin-Aein, and S. Datta, Sci. Rep. **7**, 44370 (2017).
[41] A. Khvalkovskiy, V. Cros, D. Apalkov, V. Nikitin, M. Krounbi, K. Zvezdin, A. Anane, J. Grollier, and A. Fert, Phys. Rev. B **87**, 020402 (2013).
[42] J. Torrejon, J. Kim, J. Sinha, S. Mitani, M. Hayashi, M. Yamanouchi, and H. Ohno, Nat. Commun. **5**, 4655 (2014).
[43] J. Cao, Y. Chen, T. Jin, W. Gan, Y. Wang, Y. Zheng, H. Lv, S. Cardoso, D. Wei, and W. S. Lew, Sci. Rep. **8**, 1355 (2018).
[44] C. A. Akosa, W.-S. Kim, A. Bisig, M. Kläui, K.-J. Lee, and A. Manchon, Phys. Rev. B **91**, 094411 (2015).
[45] N. Murray, W.-B. Liao, T.-C. Wang, L.-J. Chang, L.-Z. Tsai, T.-Y. Tsai, S.-F. Lee, and C.-F. Pai, Phys. Rev. B **100**, 104441 (2019).
[46] D. Pinna, F. Abreu Araujo, J.-V. Kim, V. Cros, D. Querlioz, P. Bessiere, J. Droulez, and J. Grollier, Phys. Rev. Appl. **9**, 064018 (2018).
[47] S. S. Parkin, M. Hayashi, and L. Thomas, Science **320**, 190 (2008).
[48] D. A. Allwood, G. Xiong, C. Faulkner, D. Atkinson, D. Petit, and R. Cowburn, Science **309**, 1688 (2005).
[49] J. A. Currivan-Incorvia, S. Siddiqui, S. Dutta, E. R. Evarts, J. Zhang, D. Bono, C. Ross, and M. Baldo, Nat. Commun. **7**, 10275 (2016).
[50] D. Kumar, T. Jin, R. Sbiaa, M. Kläui, S. Bedanta, S. Fukami, D. Ravelosona, S.-H. Yang, X. Liu, and S. Piramanayagam, Phys. Rep. **958**, 1 (2022).
[51] L. Thomas, M. Hayashi, X. Jiang, R. Moriya, C. Rettner, and S. S. Parkin, Nature **443**, 197 (2006).
[52] A. Manchon, J. Železný, I. M. Miron, T. Jungwirth, J. Sinova, A. Thiaville, K. Garello, and P. Gambardella, Rev. Mod. Phys. **91**, 035004 (2019).
[53] J.-G. J. Zhu and C. Park, Mater. Today **9**, 36 (2006).
[54] Q. Shao, P. Li, L. Liu, H. Yang, S. Fukami, A. Razavi, H. Wu, K. Wang, F. Freimuth, Y. Mokrousov *et al.*, IEEE Trans. Magn. **57**, 800439 (2021).
[55] S. Ikeda, J. Hayakawa, Y. Ashizawa, Y. Lee, K. Miura, H. Hasegawa, M. Tsunoda, F. Matsukura, and H. Ohno, Appl. Phys. Lett. **93**, 082508 (2008).
[56] R. Chen, Q. Cui, L. Liao, Y. Zhu, R. Zhang, H. Bai, Y. Zhou, G. Xing, F. Pan, H. Yang *et al.*, Nat. Commun. **12**, 3113 (2021).
[57] D. Wang, Z. Wang, N. Xu, L. Liu, H. Lin, X. Zhao, S. Jiang, W. Lin, N. Gao, M. Liu *et al.*, Adv. Sci. **9**, 2203006 (2022).
[58] S. Yang, J. Shin, T. Kim, K.-W. Moon, J. Kim, G. Jang, D. S. Hyeon, J. Yang, C. Hwang, Y. Jeong *et al.*, NPG Asia Mater. **13**, 11 (2021).
[59] Y. Cao, G. Xing, H. Lin, N. Zhang, H. Zheng, and K. Wang, iScience **23**, 101614 (2020).
[60] V. Sze, Y.-H. Chen, T.-J. Yang, and J. S. Emer, Proc. IEEE **105**, 2295 (2017).
[61] N. Nagaosa and Y. Tokura, Nat. Nanotechnol. **8**, 899 (2013).
[62] S. Mühlbauer, B. Binz, F. Jonietz, C. Pfleiderer, A. Rosch, A. Neubauer, R. Georgii, and P. Böni, Science **323**, 915 (2009).
[63] O. Boulle, J. Vogel, H. Yang, S. Pizzini, D. de Souza Chaves, A. Locatelli, T. O. Menteş, A. Sala, L. D. Buda-Prejbeanu, O. Klein *et al.*, Nat. Nanotechnol. **11**, 449 (2016).
[64] I. Dzyaloshinsky, J. Phys. Chem. Solids **4**, 241 (1958).
[65] K. K. Mishra, A. H. Lone, S. Srinivasan, H. Fariborzi, and G. Setti, arXiv:2308.11811 (2023).
[66] W. Legrand, D. Maccariello, N. Reyren, K. Garcia, C. Moutafis, C. Moreau-Luchaire, S. Collin, K. Bouzehouane, V. Cros, and A. Fert, Nano Lett. **17**, 2703 (2017).
[67] S. Woo, K. Litzius, B. Krüger, M.-Y. Im, L. Caretta, K. Richter, M. Mann, A. Krone, R. M. Reeve, M. Weigand *et al.*, Nat. Mater. **15**, 501 (2016).
[68] D. Pinna, G. Bourianoff, and K. Everschor-Sitte, Phys. Rev. Appl. **14**, 054020 (2020).
[69] Y. Huang, W. Kang, X. Zhang, Y. Zhou, and W. Zhao, Nanotechnology **28**, 08LT02 (2017).
[70] B. Das, J. Schulze, and U. Ganguly, IEEE Electron Device Lett. **39**, 1832 (2018).
[71] X. Chen, W. Kang, D. Zhu, X. Zhang, N. Lei, Y. Zhang, Y. Zhou, and W. Zhao, Nanoscale **10**, 6139 (2018).

[72]S. Li, W. Kang, Y. Huang, X. Zhang, Y. Zhou, and W. Zhao, Nanotechnology **28**, 31LT01 (2017).
[73]I. Lemesh and G. S. Beach, Phys. Rev. B **98**, 104402 (2018).
[74]H. Tsai, S. Ambrogio, P. Narayanan, R. M. Shelby, and G. W. Burr, J. Phys. D: Appl. Phys. **51**, 283001 (2018).
[75]T. Gokmen and Y. Vlasov, Front. Neurosci. **10**, 203376 (2016).
[76]P.-Y. Chen, X. Peng, and S. Yu, in *2017 IEEE International Electron Devices Meeting (IEDM)* (IEEE, 2017), pp. 6–1.
[77]G. Srinivasan, A. Sengupta, and K. Roy, Sci. Rep. **6**, 29545 (2016).
[78]A. Sengupta, Z. Al Azim, X. Fong, and K. Roy, Appl. Phys. Lett. **106**, 093704 (2015).
[79]A. Vansteenkiste, J. Leliaert, M. Dvornik, M. Helsen, F. Garcia-Sanchez, and B. Van Waeyenberge, AIP Adv. **4**, 107133 (2014).
[80]G. W. Burr, R. M. Shelby, A. Sebastian, S. Kim, S. Kim, S. Sidler, K. Virwani, M. Ishii, P. Narayanan, A. Fumarola *et al.*, Adv. Phys.: X **2**, 89 (2017).
[81]D. V. Christensen, R. Dittmann, B. Linares-Barranco, A. Sebastian, M. Le Gallo, A. Redaelli, S. Slesazeck, T. Mikolajick, S. Spiga, S. Menzel *et al.*, Neuromorphic Comput. Eng. **2**, 022501 (2022).
[82]N. Rathi and K. Roy, IEEE Trans. Neural Networks Learn. Syst. **34**, 3174 (2023).
[83]P. Panda, S. A. Aketi, and K. Roy, Front. Neurosci. **14**, 653 (2020).
[84]I. Lemesh, F. Büttner, and G. S. Beach, Phys. Rev. B **95**, 174423 (2017).
[85]W. Legrand, J.-Y. Chauleau, D. Maccariello, N. Reyren, S. Collin, K. Bouzehouane, N. Jaouen, V. Cros, and A. Fert, Sci. Adv. **4**, eaat0415 (2018).
[86]C. Moreau-Luchaire, C. Moutafis, N. Reyren, J. Sampaio, C. Vaz, N. Van Horne, K. Bouzehouane, K. Garcia, C. Deranlot, P. Warnicke *et al.*, Nat. Nanotechnol. **11**, 444 (2016).
[87]W. Legrand, D. Maccariello, F. Ajejas, S. Collin, A. Vecchiola, K. Bouzehouane, N. Reyren, V. Cros, and A. Fert, Nat. Mater. **19**, 34 (2020).
[88]P. Lansky, P. Sanda, and J. He, J. Comput. Neurosci. **21**, 211 (2006).
[89]D. Wang, R. Tang, H. Lin, L. Liu, N. Xu, Y. Sun, X. Zhao, Z. Wang, D. Wang, Z. Mai *et al.*, Nat. Commun. **14**, 1068 (2023).
[90]W. H. Brigner, N. Hassan, X. Hu, C. H. Bennett, F. Garcia-Sanchez, M. J. Marinella, J. A. C. Incorvia, and J. S. Friedman, in *2022 IEEE International Symposium on Circuits and Systems (ISCAS)* (IEEE, 2022), pp. 1189–1193.
[91]D. R. Rodrigues, R. Moukhader, Y. Luo, B. Fang, A. Pontlevy, A. Hamadeh, Z. Zeng, M. Carpentieri, and G. Finocchio, Phys. Rev. Appl. **19**, 064010 (2023).
[92]M. Stimberg, D. F. Goodman, V. Benichoux, and R. Brette, Front. Neuroinf. **8**, 6 (2014).
[93]N. Brunel and M. C. Van Rossum, Biol. Cybernetics **97**, 337 (2007).
[94]J. Platkiewicz and R. Brette, PLoS Comput. Biol. **6**, e1000850 (2010).
[95]L. Lapicque, J. Physiol. Paris **9**, 620 (1907).
[96]S. Ikeda, J. Hayakawa, Y. M. Lee, F. Matsukura, Y. Ohno, T. Hanyu, and H. Ohno, IEEE Trans. Electron Devices **54**, 991 (2007).
[97]S. Datta, *Quantum Transport: Atom to Transistor* (Cambridge University Press, 2005).
[98]S. Lequeux, J. Sampaio, V. Cros, K. Yakushiji, A. Fukushima, R. Matsumoto, H. Kubota, S. Yuasa, and J. Grollier, Sci. Rep. **6**, 31510 (2016).
[99]A. Sengupta and K. Roy, Appl. Phys. Rev. **4**, 041105 (2017).
[100]D. Das, Y. Cen, J. Wang, and X. Fong, Phys. Rev. Appl. **19**, 024063 (2023).
[101]I. Ribeiro de Assis, I. Mertig, and B. Göbel, Neuromorphic Comput. Eng. **3**, 014012 (2023).
[102]S. Li, A. Du, Y. Wang, X. Wang, X. Zhang, H. Cheng, W. Cai, S. Lu, K. Cao, B. Pan *et al.*, Sci. Bull. **67**, 691 (2022).
[103]N. E. Penthorn, X. Hao, Z. Wang, Y. Huai, and H. W. Jiang, Phys. Rev. Lett. **122**, 257201 (2019).
[104]S. Kasai, S. Sugimoto, Y. Nakatani, R. Ishikawa, and Y. K. Takahashi, Appl. Phys. Express **12**, 083001 (2019).
[105]K. Litzius, J. Leliaert, P. Bassirian, D. Rodrigues, S. Kromin, I. Lemesh, J. Zazvorka, K.-J. Lee, J. Mulkers, N. Kerber *et al.*, Nat. Electron. **3**, 30 (2020).
[106]J. K. Eshraghian, M. Ward, E. Neftci, X. Wang, G. Lenz, G. Dwivedi, M. Bennamoun, D. S. Jeong, and W. D. Lu, Proc. IEEE **111**, 1016 (2023).
[107]C. Lee, S. S. Sarwar, P. Panda, G. Srinivasan, and K. Roy, Front. Neurosci. **14**, 497482 (2020).
[108]S. Yaghini Bonabi, H. Asgharian, S. Safari, and M. Nili Ahmadabadi, Front. Neurosci. **8**, 379 (2014).
[109]X. Fang, S. Duan, and L. Wang, Front. Neurosci. **15**, 730566 (2021).
[110]O. I. Abiodun, A. Jantan, A. E. Omolara, K. V. Dada, N. A. Mohamed, and H. Arshad, Heliyon **4**, e00938 (2018).
[111]H. S. Seung, Neuron **40**, 1063 (2003).
[112]P. Dayan and L. F. Abbott, *Theoretical Neuroscience: Computational and Mathematical Modeling of Neural Systems* (MIT press, 2005).
[113]J. K. Eshraghian, S. Baek, J.-H. Kim, N. Iannella, K. Cho, Y. S. Goo, H. H. Iu, S.-M. Kang, and K. Eshraghian, Int. J. Neural Syst. **28**, 1850004 (2018).
[114]R. Chen, X. Wang, H. Cheng, K.-J. Lee, D. Xiong, J.-Y. Kim, S. Li, H. Yang, H. Zhang, K. Cao *et al.*, Cell Rep. Phys. Sci. **2**, 100618 (2021).
[115]F. Büttner, I. Lemesh, M. Schneider, B. Pfau, C. M. Günther, P. Hessing, J. Geilhufe, L. Caretta, D. Engel, B. Krüger *et al.*, Nat. Nanotechnol. **12**, 1040 (2017).
[116]S. Rohart and A. Thiaville, Phys. Rev. B **88**, 184422 (2013).